PONTIFICIA UNIVERSIDAD CATOLICA DE CHILE
SCHOOL OF ENGINEERING

ACTIVE REJECTION OF TERRAIN DISTURBANCES FOR HYDRAULICALLY ACTUATED MOBILE MANIPULATORS

MATTIA IGNAZIO RIGOTTI THOMPSON

Thesis submitted to the Office of Research and Graduate Studies
in partial fulfillment of the requirements for the degree of
Master of Science in Engineering

Advisor:
MIGUEL TORRES TORRITI

Santiago de Chile, May 2018

PONTIFICIA UNIVERSIDAD CATOLICA DE CHILE
SCHOOL OF ENGINEERING

ACTIVE REJECTION OF TERRAIN DISTURBANCES FOR HYDRAULICALLY ACTUATED MOBILE MANIPULATORS

MATTIA IGNAZIO RIGOTTI THOMPSON

Members of the Committee:
MIGUEL TORRES TORRITI
GIANCARLO TRONI PERALTA
FERNANDO AUAT CHEEIN
RICARDO GIESEN ENCINA

Thesis submitted to the Office of Research and Graduate Studies
in partial fulfillment of the requirements for the degree of
Master of Science in Engineering

Santiago de Chile, May 2018

Gratefully to my family, my friends,

and my grandmother Myriam

ACKNOWLEDGEMENTS

This project has been supported by the National Commission for Science and Technology Research of Chile (Conicyt) under Fondecyt grant 1171760, Fondequip grant 120141 and Basal grant FB008.

Thanks to the Robotics and Automation Laboratory (RAL) at the Pontificia Universidad Católica de Chile, specially to my advisor Miguel Torres, for his guidance through this work and the teachings he has given me personally and professionally, and to Jorge Reyes for his support and always being willing to aid me during these last years.

Also thanks to the members of the review committee for their participation in evaluating this work, and their comments and contributions during this investigation.

Finally, but most importantly, immense thanks to my parents Attilio and Myriam, to my family and to my friends, for their unconditional support and encouragement.

TABLE OF CONTENTS

LIST OF FIGURES

LIST OF TABLES

ABSTRACT

Decoupling the end-effector motion from that of the mobile base is especially important for mining mobile manipulators traversing uneven terrain, where material spillage from excavators and front-end loaders reduces productivity and slows down operations due to increased clean-up and maintenance time. Thus, this work presents an approach to actively reduce ground disturbances propagated through the wheels and arm links to the end-effector of hydraulically actuated mobile manipulators. The proposed approach is based on a combined feedforward and an $\mathcal{H}_\infty$ feedback control strategy that considers the dynamics of the hydraulic actuators, as well as the reaction forces at the contact points of the mobile base. The experimental results obtained in simulations and experimentally using an industrial semi-autonomous skid-steer loader show the effectiveness of the proposed strategy when compared to alternative disturbance reduction schemes, one based on the classic proportional-derivative (PD) control and the other on Active Disturbance Rejection Control (ADRC), with and without feedforward action. The results show that the proposed approach is able to reduce disturbances by nearly 74% when climbing over a ramp at 25% of maximum vehicle's speed, and at least by 23% when traversing over road bumps employed to replicate the effect of stones. Hence, in the context of the mining industry, the proposed strategy should help to improve existing autonomous machines that navigate with little operator intervention along mining galleries, but that are unable to avoid disturbing material on the ground or the characteristic unevenness of mining terrains.

Keywords: mobile manipulator, disturbance rejection, terrain disturbance, hydraulic actuators, $\mathcal{H}$-infinity control.

RESUMEN

El desacople entre el movimiento del extremo efector y la base móvil es especialmente importante para manipuladores móviles en minería que atraviesan terrenos disparejos, donde el derrame de material desde excavadoras y cargadores frontales reduce la productividad y enlentece las operaciones debido a un incremento en los tiempos de limpieza y mantención. Por ello, este trabajo propone un método activo de control para la reducción de perturbaciones propagadas a través de las ruedas y brazo manipulador de la máquina sobre el extremo efector de manipuladores móviles robóticos con actuadores hidráulicos. El controlador propuesto se basa en la combinación de una prealimentación calculada en tiempo real con una estrategia de control $\mathcal{H}_\infty$, que considera tanto la dinámica de los actuadores hidráulicos, como las fuerzas de reacción sobre los puntos de contacto de la base móvil. Los resultados experimentales obtenidos de simulaciones y pruebas utilizando un cargador compacto industrial semi-autónomo muestran la efectividad de la estrategia propuesta al ser comparada con estrategias de control alternativas, tales como control proporcional-derivativo (PD) clásico y *Active Disturbance Rejection Control* (ADRC), con y sin prealimentación. Los resultados demuestran que la estrategia propuesta es capaz de reducir perturbaciones cercano a un 74% conduciendo sobre una rampa a un 25% de la velocidad máxima del vehículo, y por más de un 23% conduciendo sobre resaltos ubicados en el camino para replicar el efecto de piedras. Por ello, en el contexto de la industria minera, la estrategia propuesta para la atenuación de perturbaciones debiese ayudar a mejorar la maquinaría autónoma existente, que es capaz de conducirse por galerías mineras con poca supervisión de un operador, pero no es capaz de evadir material en el terreno que genera perturbaciones o la irregularidad característica del terreno en minería.

Palabras Claves: manipulador móvil, rechazo de perturbaciones, perturbaciones de terreno, actuadores hidráulicos, control $\mathcal{H}$-infinito.

1. INTRODUCTION

1.1. Motivation

During recent years several efforts have been made to increase the level of automation and robotization of mining vehicles in order to improve productivity and safety (Paraszczak, Gustafson, & Schunnesson, 2015). Most of the developments have been focused on implementing teleoperation or autonomous navigation capabilities (Larsson, Appelgren, & Marshall, 2010). Examples of mines which at some point have made use of automated vehicles include Chilean mines Pipa Norte, Diablo Regimiento and Pilar Norte from El Teniente division, as well as mines in several countries around the world such as Australia, Canada, Finland, Sweden and South Africa (Gustafson, 2011).

However, the automation of the draw point and the efficient hauling of material requires the development of new strategies for pile handling and position control of the excavator arm capable of reducing terrain disturbances induced on the bucket position by the terrain through the wheels of the machine. Terrain disturbances along the haul path are typically caused by material that falls from the bucket of robotic mining mobile manipulators. The soil or rocks left on the path cause following machines in the convoy to drop more material as these are not avoided by teleoperated or autonomous machines. In turn, this worsens the overall performance of the production cycle, and also increases the need of maintenance on the machinery. Because of this, motor graders are frequently used for maintenance of the haul road and clearing dropped material, as presented in Fig. 1.1. This creates the inconvenience of introducing additional equipment to the work area, as well as temporarily halting production. In this context, an approach to reduce spillage through an active control method capable of reducing the effect of terrain disturbances on bucket orientation is thus necessary.

FIGURE 1.1. Motor graders used for haul road maitenance (Holman, 2006).

1.1.1. Examples

The importance of material spillage dropped on the haul road has been recognized by the mining industry. Equipment manufacturers identify spilled material and rocks as one of the main factors which contribute to tire failure in vehicles used for payload haul. Regarding tire damage, "the chief culprit is spillage from off-highway haulage trucks. It is, therefore, critical that a motor-grader is deployed on site to continually maintain haulage routes and remove loose debris" (Senyard, 2010) and "cuts and impacts are mostly caused by spillage on the haul road" (Caterpillar, n.d.).

To tackle the previous difficulties, equipment manufacturers have studied the spillage of material when traveling over uneven terrain. An example of this, as evidenced by manufacturer CAT® is presented in Fig. 1.2. Industrial loader manufacturers have recently worked on developing mechanical solutions for this problem. A common solution consists in the installation of a hydraulic accumulator which acts as a passive suspension system, reducing the rigidity of the lift boom when traveling at high speeds. Examples of this implementation include the Ride Control system patented by CAT® (A'Hearn et al., 2002) and recently implemented in their commercial loaders (Caterpillar, 2013), (Caterpillar, 2017).

FIGURE 1.2. Examples of spillage when traversing uneven terrain (Caterpillar, 2016).

It must be noted that although current passive mechanical solutions are successful in reducing vehicle vibrations and thus the consequent material spillage, these have important drawbacks. They require intervening the machinery's hydraulics circuit and the installation of additional hardware. Passive solutions are also unable to respond adequately to low frequency disturbances or changes in the vehicle's reference frame, and are thus unable to maintain a level payload when traversing slopes.

1.2. Problem Definition

The mining industry currently works with vehicles capable of autonomously hauling material. Nonetheless, these vehicles are currently not equipped to sense unevenness of the terrain and thus react appropriately to maintain a level bucket when traveling over stones, road bumps, slopes, etc. As a consequence, a portion of the hauled material is spilled and the mining process efficiency is diminished. Current solutions consist of installing passive dampeners, which require mechanical intervention of the vehicles.

Thus, as an alternative solution which does not require modification of the machine's hardware, the problem faced in this work considers the development of a control strategy for maintaining a level payload bucket on robotic mining manipulators upon the effect of external forces on the vehicle base.

1.3. Objectives

The main objective of this work is the following:

(i) Design, implementation and evaluation of a control approach for the active rejection of disturbances induced on the orientation of the end-effector of mobile robotic manipulators (specifically for an industrial front-end loader) when traversing uneven terrain.

Secondary objectives include:

(ii) Development of a dynamic model which accurately describes the position of the end-effector of a mobile robotic manipulator with hydraulic actuators, considering the effect of wheel-ground interactions when traversing uneven terrain and the dynamics of the hydraulic actuators.

(iii) Validation of the proposed model through simulations and experiments carried out on a real industrial front-end loader.

1.4. Hypothesis

A control strategy designed using an accurate model of the mobile robotic manipulator which considers the dynamic response of hydraulic actuators and the interaction between terrain, vehicle base and manipulator will be able to respond adequately to unevenness in the terrain during motion and reduce disturbances introduced to the orientation of the end-effector.

1.5. Existing Approaches

The idea of decoupling the motion of a robot arm from that of its mobile base can be traced back to the pioneering works of Dubowsky and Tanner (Dubowsky & Tanner, 1987), and by Hootsmans and Dubowsky (Hootsmans & Dubowsky, 1991). More recently, different decoupling stategies that also consider the motion dynamics of the mobile base in the control law formulation have been proposed in (Hatano, Ohsumi, Minami, & Asakura, 2000; Chi-Wu & Ke-Fei, 2009; Jimenez-Lozano & Goodwine, 2011) and (Ningyue, Liyan, & Liukeping, 2015). The latter assume that forces or torques can be directly manipulated and that the model equations describing the motion dynamics can be used to cancel nonlinearities and disturbances. However, in practice, accurate knowledge of the model parameters is difficult and forces cannot be directly used as manipulated variables, as shown in (Perrier, Cellier, & Dauchez, 1997), which studies the difficulties of force control on a real mobile robotic manipulator subject to terrain disturbances while moving. In fact, the force of typical hydraulic actuators for industrial equipment is not fully nor instantaneously adjustable because of the delays, dead zones and other nonlinearities of the servovalves. A review of the widespread applications of hydraulic actuators in robotics presented in (Mattila, Koivumki, Caldwell, & Semini, 2017) also explains the importance of considering their dynamics as part of the controller design.

The problem of keeping the end-effector tool leveled for stationary machines when raising their hydraulic manipulator arm has been considered by some authors. For example, Fales and Kelkar (Fales & Kelkar, 2005) developed a controller based on $\mathcal{H}_\infty$ techniques and evaluated the response of the nonlinear model in simulation only. A more recent study by Yung et al. (Yung, Vázquez, & Freidovich, 2015) implements a controller whose purpose is to level the bucket of a robotic front-end loader while raising the arm and the base is stationary. The proposed controller considers the active disturbance rejection approach (Han, 2009) and sliding mode control to compensate the nonlinear dynamics of the hydraulic arm. In contrast, our approach considers terrain disturbances transmitted to the end-effector of mobile manipulators in motion. Furthermore, the disturbance rejection strategy proposed here employs a feedforward action computed from joint and inertial sensor measurements combined with an end-effector position controller based on $\mathcal{H}_\infty$ feedback control design to close the control loop.

1.6. Summary of Contributions

The main contributions of this work are the following:

(i) Design and evaluation of multiple control strategies (model and non-model based) for terrain disturbance rejection on the end-effector of a mobile robotic manipulator (specifically a front-end loader used in mining).

Secondary contributions of this work include:

(ii) Integration of the actuator dynamics into a floating-base mobile manipulator model which accurately describes the dynamics of a mobile robotic manipulator with hydraulic actuators.

(iii) Validation of the developed model through simulations and data obtained from experiments carried out on an industrial semi-autonomous CAT® 262C front-end loader.

(iv) Development of a state-space representation of the above model for use in control design.

1.7. Thesis Outline

This thesis is organized as follows. Chapter 2 describes the relevant model equations for the motion dynamics of mobile manipulators, the wheel-ground interaction forces, and hydraulic actuators' dynamics; followed by a state-space representation for control design. Chapter 3 explains the proposed disturbance rejection control strategy, applied to a specific mobile manipulator, and other control strategies implemented for comparison. Chapter 4 describes the simulation and hardware implementation for the experimental setup, and the test methodology used to validate the proposed approach. Chapter 5 presents the simulation and experimental results obtained during tests with an industrial robotic mobile manipulator. Finally, Chapter 6 discusses the conclusions of the work presented, along with aspects concerning future research.

2. MODEL OF THE HYDRAULICALLY ACTUATED MOBILE MANIPULATOR

The next sections briefly explain the equations that describe the motion dynamics of the mobile manipulator, the wheel-ground interaction forces which account for the terrain-induced disturbances, and the dynamics of the hydraulic actuators.

2.1. Dynamic Equations of the Mobile Manipulator

A physically accurate model of the motion dynamics of skid-steer mobile manipulators was developed in (Aguilera-Marinovic, Torres-Torriti, & Auat-Cheein, 2017). The model considers a 6-DOF floating-base with non-permanent ground contacts on each wheel, i.e. wheels can lose contact, thus producing traction loss, as well as transmit normal reaction forces that change according to the unevenness of the terrain. Using the spatial vector algebra formalism (see (Featherstone, 2008)), the forward dynamics equations relating the base and joint accelerations can be summarized in:

$$\begin{aligned} \mathbf{a}_1 = & \underbrace{\left(\mathbf{I}_1'^{-1}\right)\mathbf{f}_{1c} + \left(\mathbf{I}_1'^{-1}\right)\sum_{i=2}^{N} {}^1\mathbf{X}_i^*\mathbf{f}_{i\,c}}_{\mathbf{a}_{1c}} - \underbrace{\left(\mathbf{I}_1'^{-1}\right)\sum_{i=2}^{N} {}^1\mathbf{X}_i^*\mathbf{f}_{i\,ext}}_{\mathbf{a}_{1/i\,ext}} \\ & - \underbrace{\left(\mathbf{I}_1'^{-1}\right)\mathbf{f}_{1ext}}_{\mathbf{a}_{1ext}}, \end{aligned} \tag{2.1}$$

$$\ddot{q}_i = \left(\tau_i - \mathbf{S}_i^T\mathbf{f}_i - \mathbf{I}_i\mathbf{S}_i\left({}^i\mathbf{X}_1\mathbf{a}_1 + \mathbf{c}_i\right)\right)\left(\mathbf{S}_i^T\mathbf{I}_i\mathbf{S}_i\right)^{-1} \tag{2.2}$$

where $\mathbf{a}_1$ is the spatial acceleration of the mobile base, $\ddot{q}_i$ is the joint acceleration of the manipulator's i-th body, $\mathbf{S}_i$ is the i-th joint motion subspace matrix, $\mathbf{I}_i$ is the spatial inertia of the body i, $\mathbf{I}_i'$ is the total spatial inertia of the body i including the children bodies' inertia, ${}^j\mathbf{X}_i$ and ${}^j\mathbf{X}_i^*$ are the link i to link j motion and force transforms, respectively. The term $\mathbf{c}_i$ is the i-th joint spatial acceleration due to velocity product terms, $\mathbf{f}_{1c}$ is the spatial force due to the velocity-product terms and $\mathbf{f}_{1ext}$ is the external force on the base. Similarly, the external forces acting on the i-th link of the arm are represented by $\mathbf{f}_i$, while τ_i is the torque applied to joint i. The traction and normal reaction forces acting on the wheels are included in $\mathbf{f}_{1ext}$. A labeled diagram for the front-end loader model is presented in Fig. 2.1. For further details see (Aguilera-Marinovic et al., 2017).

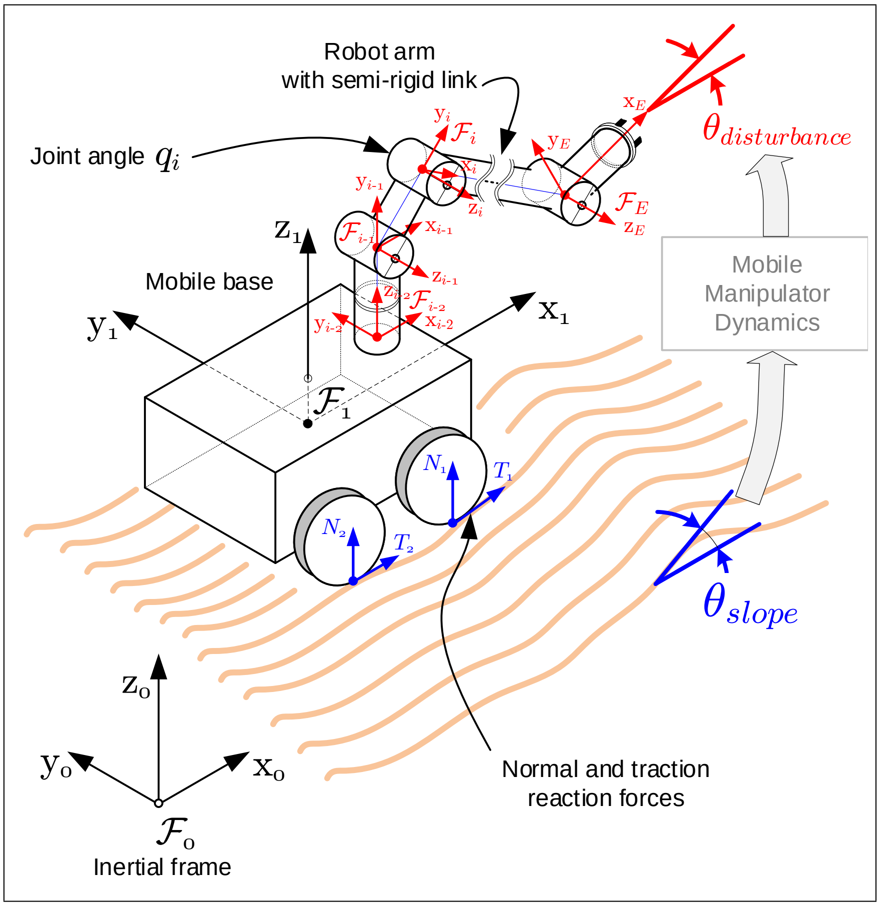

FIGURE 2.1. Mobile robotic manipulator with wheel-ground interactions.

2.2. Wheel-Ground Interaction

The wheel-ground interaction forces comprehend a tangential and a normal reaction force. The terrain is treated as a deformable surface and the wheels have contact points that can sink or separate from the ground. The tangential reaction is related to the tractive force and the torque applied by the wheels, while the normal force is related to the weight and unevenness of the terrain. For a detailed explanation please refer to (Aguilera-Marinovic et al., 2017). Changes in the normal force that occur when the machine drives over potholes, mounds or debris are some of the main causes of disturbances propagated through the wheels to the load on the arm. The normal force N acting over each contact point is based on the Hunt-Crossley model (Gilardi & Sharf, 2002), which describes the surface as a deformable first-order massless system. The magnitude of the normal reaction force is computed from the equation:

$$N = -K_N \delta^n - D_N \delta^p \dot{\delta}^q \tag{2.3}$$

where δ is the contact point surface penetration distance, K_N and D_N are surface stiffness and damping coefficients, respectively. Here, $n = 3/2$, $p = 1/2$ and $q = 1$ are used following (Azad & Featherstone, 2014). On each active contact point of the wheel, the external forces include a normal component in the form of (2.3), that make up the total external force acting on the base $\mathbf{f}_{1ext}$ affecting the acceleration of the mobile base (2.1).

2.3. Hydraulic Actuator Dynamics and Applied Torque

Industrial machinery capable of lifting heavy loads typically employ bi-chamber hydraulic cylinders with servovalves, see Fig. 2.2, to manipulate the oil flow. The net force F applied by a bi-chamber hydraulic actuators is determined by the pressure difference between each side of the cylinder, minus the friction due to fluid viscosity:

$$F = \Delta P \cdot \bar{A} - \mu_v \dot{\delta} \tag{2.4}$$

where $\Delta P = P_\mathrm{A} - P_\mathrm{B}$ is the pressure difference between chambers A and B of the cylinder, and $\bar{A}$ is the effective area on which the pressure P_k, $k = \mathrm{A}, \mathrm{B}$, acts to produce work, μ_v is the viscous friction coefficient, and $\dot{\delta}$ is the actuator's displacement speed. The force F_i of the i-th actuator produces a torque that adjusts the i-th joint acceleration given in (2.2) according to

$$\tau_i = F_i \, r_i \sin(\theta_i + q_i), \tag{2.5}$$

where r_i is the distance from the joint to the point at which force F_i is applied by the actuator, q_i is the joint angle, and $\theta_i + q_i$ is the angle of incidence at which the force is applied on the arm link. The value of θ_i depends on specific mounting geometry.

The servovalves employed to manipulate the flows Q_k, $k = \mathrm{A, B}$, into the chambers of the cylinder introduce additional nonlinearities in the relation between the valve's input signal and the output torque due to different aspects, such as fluid compressibility, pressure drops in variable section orifices, and lags (Efe, 2014), (Yang, Zheng, & Chen, 2018), (Yung et al., 2015). The main aspects that influence the dynamics of hydraulic actuators are discussed next.

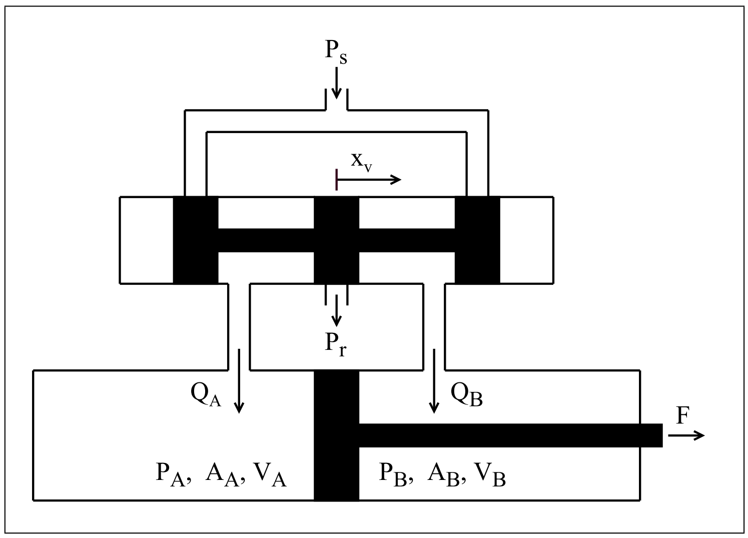

FIGURE 2.2. Bi-chamber hydraulic actuator and servovalve system.

2.3.1. Fluid Compressibility

The dynamic equation describing the pressures P_k, $k = \mathrm{A, B}$, in (2.4) is given by:

$$\dot{P}_k = \frac{\beta}{V_k}\left(Q_k - \dot{V}_k\right), \quad k = \mathrm{A, B} \tag{2.6}$$

where β is the bulk modulus, V_k is the volume and Q_k is the net flow of the fluid in chamber $k = \mathrm{A, B}$ of the cylinder. The bulk modulus β associated to the fluid's compressibility is influenced by several factors, such as entrained air, temperature and fluid pressure. However, here β is assumed to be constant considering that temperature stays relatively constant and at high pressures the effect of entrained air is negligible (Efe, 2014).

2.3.2. Servovalve Flow

The flow Q_{A} from (2.6) through the valve orifice for chamber A may be described by:

$$Q_{\mathrm{A}} = \begin{cases} c_v O(x_v)\sqrt{\frac{2}{\rho}(P_{\mathrm{s}} - P_{\mathrm{A}})} & x_v < 0 \\ -c_v O(x_v)\sqrt{\frac{2}{\rho}(P_{\mathrm{A}} - P_{\mathrm{r}})} & x_v \geq 0 \end{cases} \tag{2.7}$$

where c_v is the flow coefficient, x_v is the servovalve displacement, $O(x_v)$ is the valve opening depending on its displacement, ρ is the fluid density and P_{s}, P_{r} are the supply and reservoir pressures.

For chamber B the equations are similar, but the flow is reversed in terms of valve displacement x_v:

$$Q_{\mathrm{B}} = \begin{cases} -c_v O(x_v)\sqrt{\frac{2}{\rho}(P_{\mathrm{B}} - P_{\mathrm{r}})} & x_v < 0 \\ c_v O(x_v)\sqrt{\frac{2}{\rho}(P_{\mathrm{s}} - P_{\mathrm{B}})} & x_v \geq 0 \end{cases} \tag{2.8}$$

2.3.3. Servovalve Position

The hydraulic actuator flow is adjusted by the displacement of the servovalve, which is regulated by a current input. The displacement of the servovalve's spool modifies the cross-section of the orifice in a highly nonlinear way due to different reasons; see (Efe, 2014) for an in-depth study. Sources of undesired nonlinear response include the valve's dead-zone, orifice shape and hysteresis. The reaction time of the servovalve is another important aspect, which is modeled using a first order lag with time constant T_v.

2.4. State-Space Representation

The state-space representation of the hydraulically actuated robotic mobile manipulator employed in the formulation of the disturbance rejection strategies considers a state vector composed of the mobile base tilt angle θ and tilt rate $\dot{\theta}$, the $2N$ states corresponding to the angular position and velocity q_i, $\dot{q}_i$ of the N joints of the manipulator arm, and $2N_A$ states associated to the N_A hydraulic actuators.

The state-space representation admits both actuated and non-actuated joints, thus $N_A \leq N$. Non-actuated joints are employed here to represent semi-rigid arm links that have small deflectations and vibrate like cantilevered beams. The non-actuated joints consider dampened spring-like forces with stiffness and damping coefficients K_C and D_C, which preserve a steady-state static link position and are adjusted to the resonance frequency of the arm link. Thus by substitution of (2.4) into (2.5) and the latter, the torque applied to joint i, for the actuated and non-actuated case, is given by:

$$\tau_i = \begin{cases} (\Delta P_i \cdot \bar{A} - \mu_v \dot{\delta}_i)\, r_i \sin(\theta_i + q_i) & i \in \mathcal{I}_A \\ -K_C q_i - D_C \dot{q}_i & i \in \mathcal{I}_P \end{cases} \tag{2.9}$$

where $\mathcal{I}_A$ and $\mathcal{I}_P$ are the sets of indexes of actuated and non-actuated passive joints, respectively.

The state-space model equations for each manipulator joint is obtained substituting (2.9) into (2.2). Each actuated joint is associated to two additional hydraulic actuator states corresponding to the pressure difference $\Delta P = P_{\mathrm{A}} - P_{\mathrm{B}}$ between chambers A and B, and the servovalve position x_v. The corresponding state equations are obtained replacing (2.7) and (2.8) in (2.6). The state-space representation (2.10) is obtained by linearizing the mentioned state equations about an equilibrium point $\boldsymbol{x}_e$ corresponding to a horizontally leveled end-effector. Input matrix $\boldsymbol{B}$ is separated into disturbance and control inputs: the first column corresponds to the base angular acceleration disturbance input $a_{1,\theta}$, the component of $\mathbf{a}_1$ in (2.2) acting on the tilt axis θ, and the remaining columns corresponds to the control inputs $\boldsymbol{u}$, representing the input currents which operate the actuator servovalves.

$$
\boldsymbol{A} = \left. \left[\begin{array}{cc:ccccc:ccccc}
0 & 1 & 0 & 0 & \cdots & 0 & 0 & 0 & 0 & \cdots & 0 & 0 \\
0 & 0 & 0 & 0 & \cdots & 0 & 0 & 0 & 0 & \cdots & 0 & 0 \\
\hdashline
0 & 0 & 0 & 1 & \cdots & 0 & 0 & 0 & 0 & \cdots & 0 & 0 \\
0 & 0 & \frac{\delta \ddot{q}_2}{\delta q_2} & \frac{\delta \ddot{q}_2}{\delta \dot{q}_2} & \cdots & \frac{\delta \ddot{q}_2}{\delta q_N} & \frac{\delta \ddot{q}_2}{\delta \dot{q}_N} & \frac{\delta \ddot{q}_2}{\delta \Delta P_2} & 0 & \cdots & \frac{\delta \ddot{q}_2}{\delta \Delta P_N} & 0 \\
\vdots & \vdots & \vdots & \vdots & \ddots & \vdots & \vdots & \vdots & \vdots & \ddots & \vdots & \vdots \\
0 & 0 & 0 & 0 & \cdots & 0 & 1 & 0 & 0 & \cdots & 0 & 0 \\
0 & 0 & \frac{\delta \ddot{q}_N}{\delta q_2} & \frac{\delta \ddot{q}_N}{\delta \dot{q}_2} & \cdots & \frac{\delta \ddot{q}_N}{\delta q_N} & \frac{\delta \ddot{q}_N}{\delta \dot{q}_N} & \frac{\delta \ddot{q}_N}{\delta \Delta P_2} & 0 & \cdots & \frac{\delta \ddot{q}_N}{\delta \Delta P_N} & 0 \\
\hdashline
0 & 0 & 0 & \frac{\delta \Delta P_2}{\delta \dot{q}_2} & \cdots & 0 & \frac{\delta \Delta P_2}{\delta \dot{q}_N} & 0 & \frac{\delta \Delta P_2}{\delta x_{v2}} & \cdots & 0 & 0 \\
0 & 0 & 0 & 0 & \cdots & 0 & 0 & 0 & -T_{v2}^{-1} & \cdots & 0 & 0 \\
\vdots & \vdots & \vdots & \vdots & \ddots & \vdots & \vdots & \vdots & \vdots & \ddots & \vdots & \vdots \\
0 & 0 & 0 & \frac{\delta \Delta P_N}{\delta \dot{q}_2} & \cdots & 0 & \frac{\delta \Delta P_N}{\delta \dot{q}_N} & 0 & 0 & \cdots & 0 & \frac{\delta \Delta P_N}{\delta x_{vN}} \\
0 & 0 & 0 & 0 & \cdots & 0 & 0 & 0 & 0 & \cdots & 0 & -T_{vN}^{-1}
\end{array}\right] \right|_{\boldsymbol{x}_e}
\begin{array}{l}
\left.\begin{array}{c} \\ \\ \end{array}\right\} \text{vehicle base tilt} \\
\left.\begin{array}{c} \\ \\ \\ \\ \\ \end{array}\right\} \text{joint dynamics} \\
\left.\begin{array}{c} \\ \\ \\ \\ \\ \end{array}\right\} \text{actuator dynamics}
\end{array}
\tag{2.10}
$$

$$
\boldsymbol{B} = \left. \left[\begin{array}{c|ccc}
0 & 0 & \cdots & 0 \\
1 & 0 & \cdots & 0 \\
\hdashline
0 & 0 & \cdots & 0 \\
\frac{\delta \ddot{q}_2}{\delta a_{1,\theta}} & 0 & \cdots & 0 \\
\vdots & \vdots & \ddots & \vdots \\
0 & 0 & \cdots & 0 \\
\frac{\delta \ddot{q}_N}{\delta a_{1,\theta}} & 0 & \cdots & 0 \\
\hdashline
0 & 0 & \cdots & 0 \\
0 & T_{v2}^{-1} & \cdots & 0 \\
\vdots & \vdots & \ddots & \vdots \\
0 & 0 & \cdots & 0 \\
0 & 0 & \cdots & T_{vN}^{-1}
\end{array}\right] \right|_{\boldsymbol{x}_e}
\begin{array}{l}
\left.\begin{array}{c} \\ \\ \end{array}\right\} \text{vehicle base tilt} \\
\left.\begin{array}{c} \\ \\ \\ \\ \\ \end{array}\right\} \text{joint dynamics} \\
\left.\begin{array}{c} \\ \\ \\ \\ \\ \end{array}\right\} \text{actuator dynamics}
\end{array}
$$

3. CONTROL DESIGN

The proposed disturbance rejection strategy is defined as a control law:

$$\boldsymbol{u}(\boldsymbol{x},t) \;\; = \;\; \boldsymbol{u}_{\infty}(\boldsymbol{x},t) + \boldsymbol{u}_{\mathit{ff}}(t) \tag{3.1}$$

where $\boldsymbol{u}_{\infty}(\boldsymbol{x},t)$ is an $\mathcal{H}_{\infty}$ feedback controller and $\boldsymbol{u}_{\mathit{ff}}(t)$ is a feedforward action obtained from the measurement of the pitch rate of the mobile base. Alternative feedback controllers, which include one based on the classic PD control, and another based on the Active Disturbance Rejection Controller (ADRC) (Gao, 2006; Han, 2009) are also implemented for benchmarking purposes. The implementation of the ADRC and $\mathcal{H}_{\infty}$ controllers, as well as the feedforward action is explained next.

3.1. Active Disturbance Rejection Control

The Active Disturbance Rejection Control method (ADRC) (Gao, 2006; Han, 2009) has become prominent in recent years as a means to reduce the effect of system disturbances. ADRC is based on the concept that a system's nonlinearities, internal parameter uncertainties and external disturbances may be directly eliminated through control action. To this end, the system dynamics described by equations (2.1) and (2.2) is reduced to the end-effector joint and approximated by a second order model of the form:

$$\begin{aligned} \dot{\zeta}_1 &= \zeta_2 \\ \dot{\zeta}_2 &= g(\boldsymbol{\zeta},u,d) + bu + d \\ y &= \zeta_1 \end{aligned} \tag{3.2}$$

where $g(\boldsymbol{\zeta},u,d)$ represents the model nonlinearities and uncertainties, u is the control input, b is the input gain (measured experimentally) and d are external disturbances. The states $\boldsymbol{\zeta} = [\zeta_1,\ \zeta_2,\ \zeta_3]^T$ are virtual states which represent the reduced system's simplified second order dynamic response.

The disturbance $f = d + g(\boldsymbol{\zeta},u,d)$ in equation (3.2) may be eliminated by a control action of the form $u = b^{-1}(u_0 - f)$, provided an accurate estimation of f can be computed (see (Gao, 2006; Han, 2009)), and u_0 is a stabilizing feedback control law. In order to estimate f, the following extended state observer is proposed in (Gao, 2006):

$$\begin{aligned}
\dot{\hat{\zeta}}_1 &= \hat{\zeta}_2 + L_1(y - \hat{\zeta}_1) \\
\dot{\hat{\zeta}}_2 &= bu + \hat{\zeta}_3 + L_2(y - \hat{\zeta}_1) \\
\dot{\hat{\zeta}}_3 &= L_3(y - \hat{\zeta}_1)
\end{aligned} \tag{3.3}$$

where $\hat{\zeta}_3$ corresponds to the estimate of total disturbance f, and $L_1 = 3\omega_0$, $L_2 = 3\omega_0^2$ and $L_3 = \omega_0^3$ are the observer gains that set all observer poles at a cutoff frequency ω_0 as suggested in (Gao, 2003). Here an observer bandwidth of $\omega_0 = 5$ rad/s is used.

A PD controller is implemented to compute the stabilizing feedback u_0. Since the target output is a leveled bucket, i.e. the desired value for the bucket's orientation with respect to the ground plane is $y^d = \theta + q_1 + q_2 = 0$, the error between the desired and measured tilt is given by $e = y^d - y = -y$, and thus the control law is given by:

$$u_{ADRC} = \frac{1}{b}\left(-bK_p y - \frac{bK_d}{sT_f + 1}\dot{y} - \alpha\hat{\zeta}_3\right) \tag{3.4}$$

The PD control parameters are manually tuned for a fast tracking of the step changes in the base angle θ while ensuring a minimal overshoot when applied to the real industrial loader. Good results were obtained using gains $K_p = 200$ and $K_d = 20$, with a derivative action cutoff frequency of 10 Hz, which results in $T_f = 0.0159$ s. The implemented ADRC control presented stability issues in practice, which where solved by scaling the estimated disturbance $\hat{\zeta}_3$ fed to the controller by $\alpha < 1$. An input gain of $b = 8.25 \cdot 10^{-3}$ and scaling factor of $\alpha = 0.25$ were used in the experiments.

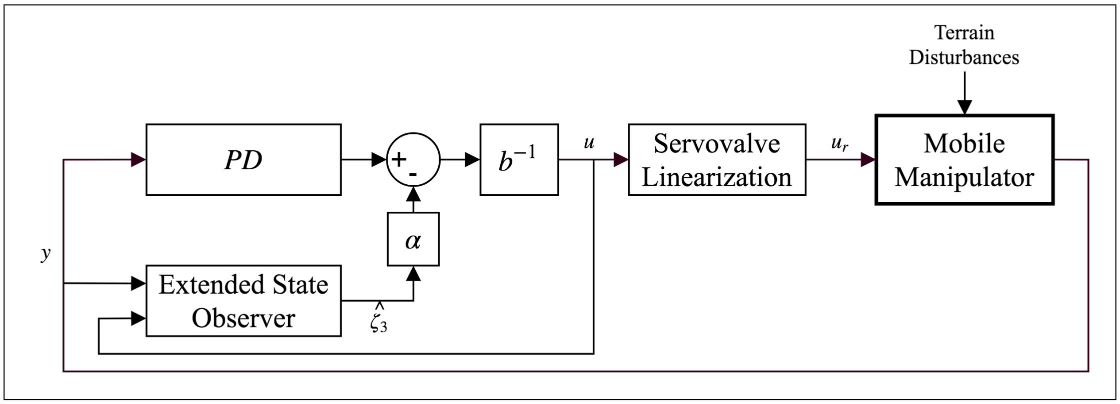

FIGURE 3.1. ADRC control scheme.

3.2. $\mathcal{H}_\infty$ Control

$\mathcal{H}_\infty$ control methods were first introduced by George Zames (Zames, 1981) and constitute one of the classical methods for designing controllers which minimize the effect of disturbances on the closed-loop system. These methods are model-based, and compute the controller by solving an optimization problem which minimizes the $\mathcal{H}_\infty$ norm of the closed-loop system, which is equivalent to the maximum magnitude of the frequency response for single-input, single-output systems. The methods commonly used for numerical computation of the $\mathcal{H}_\infty$ optimal control problem solution were proposed by (Glover & Doyle, 1988) and (Doyle, Glover, Khargonekar, & Francis, 1989). In the following sections, the theory behind the $\mathcal{H}_\infty$ optimal control problem and its solution will first be described in 3.2.1, based on notes by (Toivonen, 1998). Sections 3.2.2 and 3.2.3 will present the model equations used, based on the state-space representation presented previously, and the $\mathcal{H}_\infty$ controller design itself.

3.2.1. $\mathcal{H}_\infty$ Optimal Control Problem

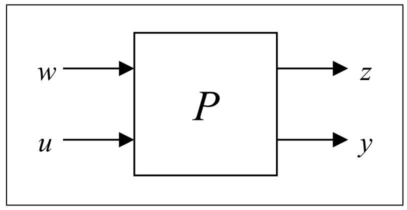

FIGURE 3.2. Partitioned plant $\boldsymbol{P}$.

Consider a partitioned plant $\boldsymbol{P}$ (Fig. 3.2) and its state-space representation:

$$\begin{aligned}\dot{\boldsymbol{x}} &= \boldsymbol{A}\boldsymbol{x} + \boldsymbol{B}_1\boldsymbol{w} + \boldsymbol{B}_2\boldsymbol{u} \\ \boldsymbol{z} &= \boldsymbol{C}_1\boldsymbol{x} + \boldsymbol{D}_{11}\boldsymbol{w} + \boldsymbol{D}_{12}\boldsymbol{u} \\ \boldsymbol{y} &= \boldsymbol{C}_2\boldsymbol{x} + \boldsymbol{D}_{21}\boldsymbol{w} + \boldsymbol{D}_{22}\boldsymbol{u}\end{aligned} \tag{3.5}$$

where $\boldsymbol{w}$ is the disturbance input, $\boldsymbol{u}$ the control input, $\boldsymbol{z}$ the performance output, and $\boldsymbol{y}$ the measured output. The $\mathcal{H}_\infty$ optimal control problem aims to obtain a controller $\boldsymbol{K}$ such that the $\mathcal{H}_\infty$ norm (3.6) of the closed loop system $\boldsymbol{T}$ (Fig. 3.3) is minimized.

$$\|\boldsymbol{T}\|_{\mathcal{H}_\infty} = \sup_{\boldsymbol{w}\neq 0} |\boldsymbol{T}(j\omega)| \tag{3.6}$$

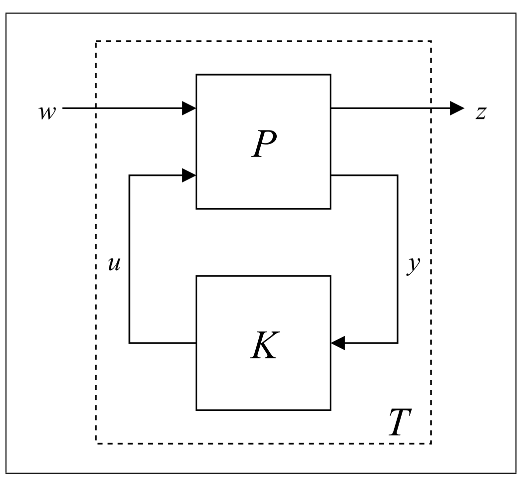

FIGURE 3.3. Closed loop system $\boldsymbol{T}$.

Note that due to Parseval's Theorem, (3.6) is equivalent in the time domain to:

$$\|\boldsymbol{T}\|_{\mathcal{H}_\infty} = \sup_{\boldsymbol{w} \neq 0} \frac{\|\boldsymbol{z}\|_{\mathcal{L}_2}}{\|\boldsymbol{w}\|_{\mathcal{L}_2}} \tag{3.7}$$

where the $\mathcal{L}_2$ norm of a time signal x corresponds to:

$$\|x\|_{\mathcal{L}_2} = \left(\int_0^\infty x(t)^2 dt \right)^{1/2} \tag{3.8}$$

Computing a controller $\boldsymbol{K}$ which directly minimizes the norm (3.7) is a challenging and a computationally demanding problem. Commonly used algorithms approach this optimization problem by iteratively solving a sub-optimal problem for which the computed controller satisfies:

$$\frac{\|\boldsymbol{z}\|_{\mathcal{L}_2}}{\|\boldsymbol{w}\|_{\mathcal{L}_2}} < \gamma, \quad \forall\, \boldsymbol{w} \neq 0 \tag{3.9}$$

or its equivalent:

$$\|\boldsymbol{z}\|^2_{\mathcal{L}_2} - \gamma^2 \|\boldsymbol{w}\|^2_{\mathcal{L}_2} < 0, \quad \forall\, \boldsymbol{w} \neq 0 \tag{3.10}$$

which may be rewritten as:

$$\int_0^\infty \left(\boldsymbol{z}(t)^T \boldsymbol{z}(t) - \gamma^2 \boldsymbol{w}(t)^T \boldsymbol{w}(t) \right) dt < 0, \quad \forall\, \boldsymbol{w} \neq 0 \tag{3.11}$$

The sub-optimal $\mathcal{H}_\infty$ control problem is thus solved in the time domain in the form of a linear quadratic game problem derived from (3.11).

The linear quadratic problem is solved through two Ricatti equations, which respectively solve an $\mathcal{H}_\infty$ optimal estimation problem and $\mathcal{H}_\infty$ optimal state feedback problem. The following conditions are assumed, to simplify the problem solution:

(i) The pair $(\boldsymbol{A}, \boldsymbol{B}_1)$ is stabilizable and the pair $(\boldsymbol{C}_2, \boldsymbol{A})$ is detectable.

(ii) $\boldsymbol{D}_{21}\boldsymbol{D}_{21}^T$ is invertible and $\boldsymbol{D}_{21}\boldsymbol{B}_1^T = 0$.

(iii) The pair $(\boldsymbol{A}, \boldsymbol{B}_2)$ is stabilizable and the pair $(\boldsymbol{C}_1, \boldsymbol{A})$ is detectable.

(iv) $\boldsymbol{D}_{12}^T\boldsymbol{D}_{12}$ is invertible and $\boldsymbol{D}_{12}^T\boldsymbol{C}_1 = 0$.

If the mentioned conditions hold, there exists a controller which satisfies the equivalent bounds (3.9) and (3.11) if there exists a stabilizing solution $\boldsymbol{Y} \geq 0$ to the $\mathcal{H}_\infty$ optimal estimation Ricatti equation (3.12), a stabilizing solution $\boldsymbol{X} \geq 0$ to the Ricatti equation related to the $\mathcal{H}_\infty$ optimal state feedback problem (3.13), and the matrix $\gamma^2 \boldsymbol{I} - \boldsymbol{Y}\boldsymbol{X}$ is positive definite.

$$\boldsymbol{A}\boldsymbol{Y} + \boldsymbol{Y}\boldsymbol{A}^T - \boldsymbol{Y}\boldsymbol{C}_2^T \left(\boldsymbol{D}_{21}\boldsymbol{D}_{21}^T\right)^{-1} \boldsymbol{C}_2\boldsymbol{Y} + \gamma^{-2}\boldsymbol{Y}\boldsymbol{C}_1^T\boldsymbol{C}_1\boldsymbol{Y} + \boldsymbol{B}_1\boldsymbol{B}_1^T = 0 \tag{3.12}$$

$$\boldsymbol{A}^T\boldsymbol{X} + \boldsymbol{X}\boldsymbol{A} - \boldsymbol{X}\boldsymbol{B}_2 \left(\boldsymbol{D}_{12}^T\boldsymbol{D}_{12}\right)^{-1} \boldsymbol{B}_2^T\boldsymbol{X} + \gamma^{-2}\boldsymbol{X}\boldsymbol{B}_1\boldsymbol{B}_1^T\boldsymbol{X} + \boldsymbol{C}_1^T\boldsymbol{C}_1 = 0 \tag{3.13}$$

The γ-iteration $\mathcal{H}_\infty$ sub-optimal controller $\boldsymbol{K}$ is thus given by:

$$\begin{aligned} \dot{\hat{\boldsymbol{x}}} &= \left(\boldsymbol{A} + \gamma^{-2}\boldsymbol{B}_1\boldsymbol{B}_1^T\boldsymbol{X} - \boldsymbol{B}_2\left(\boldsymbol{D}_{12}^T\boldsymbol{D}_{12}\right)^{-1}\boldsymbol{B}_2^T\boldsymbol{X} - \boldsymbol{L}_Z\left(\boldsymbol{C}_2 + \gamma^{-2}\boldsymbol{D}_{21}\boldsymbol{B}_1^T\boldsymbol{X}\right)\right)\hat{\boldsymbol{x}} + \boldsymbol{L}_Z\boldsymbol{y} \\ \boldsymbol{u} &= -\left(\boldsymbol{D}_{12}^T\boldsymbol{D}_{12}\right)^{-1}\boldsymbol{B}_2^T\hat{\boldsymbol{x}} \end{aligned} \tag{3.14}$$

with $\boldsymbol{L}_Z = \boldsymbol{Y}\left(\boldsymbol{I} - \gamma^{-2}\boldsymbol{X}\boldsymbol{Y}\right)^{-1}\left(\boldsymbol{C}_2 + \gamma^{-2}\boldsymbol{D}_{21}\boldsymbol{B}_1^T\boldsymbol{X}\right)^T(\boldsymbol{D}_{21}\boldsymbol{D}_{21}^T)^{-1}$.

3.2.2. State Equations

The mobile manipulator model employed in the design of the controller corresponds to the one described in Section 2, with a two-link arm configuration equivalent to that of front-end loaders and parameters summarized in Table 3.1. The state-space representation defined in (2.10) has an 8-dimensional state vector $\boldsymbol{x}$, where x_1, x_2 are the base pitch and pitch rate; x_3, x_4 are the arm link angular position and velocity; x_5, x_6 are the bucket link angular position and velocity, x_7 is the pressure difference between chambers of the bucket link hydraulic actuator, and x_8 is the servovalve's position. The first joint is treated as a non-actuated passive joint with spring and damping coefficients K_C and D_C of equation (2.9) set to match the measured main vibration frequency of the first link, which was approximately 1.6 Hz. The second joint that moves the excavator bucket is actuated to compensate the ground disturbances.

It must be noted that minor modifications must be made to the obtained linearized model such that requirements are met for the solution of the $\mathcal{H}_\infty$ optimal control problem. Due to states x_1 and x_2 comprising a double integrator of the input base acceleration

TABLE 3.1. Model parameters.

Parameters	Values (in SI units)
$\mathbf{I}_1$ (base)	$\frac{1}{12}m_1 \,\mathrm{diag}\,(1.6^2 + 1.2^2, 3^2 + 1.2^2, 3^2 + 1.6^2)$
$\mathbf{I}_2$ (arm)	$\frac{1}{12}m_2 \,\mathrm{diag}\,(0.2^2 + 0.3^2, 3.3^2 + 0.3^2, 3.3^2 + 0.2^2)$
$\mathbf{I}_3$ (bucket)	$\frac{1}{12}m_3 \,\mathrm{diag}\,(1.8^2 + 0.02^2, 1^2 + 0.02^2, 1^2 + 1.8^2)$
m_1	2389
m_2	834
m_3	300
K_N	$1500 \cdot 10^3$
D_N	$200 \cdot 10^3$
A	$8 \cdot 10^{-3}$
μ_v	500
β	$1.8 \cdot 10^9$
ρ	857
c_v	$2.919 \cdot 10^{-4}$
$P_s - P_r$	$23000 \cdot 10^3$
T_v	0.15
K_C	$0.5 \cdot 10^6$
D_C	$2 \cdot 10^3$

disturbances, the pair $(\boldsymbol{A}, \boldsymbol{B}_2)$ is not stabilizable. To solve this issue, the second state space equation is altered by adding a virtual low frequency restitution force as follows:

$$\dot{x}_2 = -1 \cdot 10^{-4} x_1 - 0.25 \cdot 10^{-8} x_2 + a_{1,\theta} \tag{3.15}$$

Thus these states become controllable without significantly modifying the modeled system dynamics (the added restitution force is negligible in comparison to other involved forces).

3.2.3. Proposed $\mathcal{H}_\infty$ Control Design

The measured variables available to the $\mathcal{H}_\infty$ controller are:

$$y = \left[\begin{array}{c} x_1 + x_3 + x_5 \end{array}\right] = \left[\begin{array}{c} \theta + q_1 + q_2 \end{array}\right] \tag{3.16}$$

It is to be noted that the output variable $x_1 + x_3 + x_5$ is computed directly from the inclinometer located on the bucket, which measures the bucket tilt angle with respect to the gravity vector. The performance output considered for the controller design is defined as:

$$\boldsymbol{z}_\infty = \begin{bmatrix} x_1 + x_3 + x_5 \\ Du \end{bmatrix} \tag{3.17}$$

Also, an additional disturbance input is defined, such that the condition for $\boldsymbol{D}_{21}\boldsymbol{D}_{21}^T$ being invertible is satisfied. This new disturbance corresponds to the sensor noise, and its respective coefficient in matrix $\boldsymbol{D}_{21}$ is set in relation to the relative magnitude between the tilt sensor measurement and noise. The partitioned plant representation (3.5) used for control design is presented in (3.18).

$$\begin{gathered}
\boldsymbol{A} = \begin{bmatrix} 0 & 1 & 0 & 0 & 0 & 0 & 0 & 0 \\ -2.500\text{e}{-9} & -1.000\text{e}{-4} & 0 & 0 & 0 & 0 & 0 & 0 \\ 0 & 0 & 0 & 1 & 0 & 0 & 0 & 0 \\ 0 & 0 & -3.629\text{e}2 & -1.458\text{e}0 & 3.864\text{e}0 & 4.209\text{e}0 & -2.816\text{e}{-5} & 0 \\ 0 & 0 & 0 & 0 & 0 & 1 & 0 & 0 \\ 0 & 0 & 2.087\text{e}3 & 8.417\text{e}0 & -3.148\text{e}1 & -3.429\text{e}1 & 2.294\text{e}-4 & 0 \\ 0 & 0 & 0 & 0 & 0 & -1.486\text{e}9 & 0 & 1.260\text{e}5 \\ 0 & 0 & 0 & 0 & 0 & 0 & 0 & -6.667\text{e}0 \end{bmatrix} \\
\boldsymbol{B}_1 = \begin{bmatrix} 0 & 0 \\ 1 & 0 \\ 0 & 0 \\ -3.459\text{e}{-1} & 0 \\ 0 & 0 \\ -1.975\text{e}0 & 0 \\ 0 & 0 \\ 0 & 0 \end{bmatrix} \quad \boldsymbol{B}_2 = \begin{bmatrix} 0 \\ 0 \\ 0 \\ 0 \\ 0 \\ 0 \\ 0 \\ 6.667\text{e}0 \end{bmatrix} \\
\boldsymbol{C}_1 = \begin{bmatrix} 1 & 0 & 1 & 0 & 1 & 0 & 0 & 0 \\ 0 & 0 & 0 & 0 & 0 & 0 & 0 & 0 \end{bmatrix} \quad \boldsymbol{D}_{11} = \begin{bmatrix} 0 & 0 \\ 0 & 0 \end{bmatrix} \quad \boldsymbol{D}_{12} = \begin{bmatrix} 0 \\ D \end{bmatrix} \\
\boldsymbol{C}_2 = \begin{bmatrix} 1 & 0 & 1 & 0 & 1 & 0 & 0 & 0 \end{bmatrix} \quad \boldsymbol{D}_{21} = \begin{bmatrix} 0 & 1\text{e}{-2} \end{bmatrix} \quad \boldsymbol{D}_{22} = \begin{bmatrix} 0 \end{bmatrix}
\end{gathered} \tag{3.18}$$

The $\mathcal{H}_\infty$ problem of finding a controller of the form $u_\infty = \boldsymbol{K} * y$, where $\boldsymbol{K}$ is a dynamic feedback controller that minimizes the energy gain, i.e. that minimizes the closed-loop transfer matrix from disturbance input $a_{1,\theta}$ to the performance output $\boldsymbol{z}_\infty$:

$$\|\boldsymbol{T}_{\boldsymbol{z}_\infty, a_{1,\theta}}\|_{\mathcal{H}_\infty} = \sup_{a_{1,\theta} \neq 0} \frac{\|\boldsymbol{z}_\infty\|_{\mathcal{L}_2}}{\|a_{1,\theta}\|_{\mathcal{L}_2}} \tag{3.19}$$

is solved using the two-Riccati formulae described in Section 3.2 and the standard γ-iteration technique based on the bisection algorithm implemented in (Balas, Chiang, Packard, & Safonov, 2015). The resulting controller is implemented as a dynamical system:

$$\begin{aligned}\dot{\hat{\boldsymbol{x}}}_\infty &= \hat{\boldsymbol{A}}_\infty \hat{\boldsymbol{x}}_\infty + \hat{\boldsymbol{B}}_\infty y \\ u_\infty &= \hat{\boldsymbol{C}}_\infty \hat{\boldsymbol{x}}_\infty \end{aligned} \tag{3.20}$$

with input y, output u_∞, internal states $\hat{\boldsymbol{x}}_\infty$ and state-space matrices $\hat{\boldsymbol{A}}_\infty, \hat{\boldsymbol{B}}_\infty, \hat{\boldsymbol{C}}_\infty$ given in (3.21).

$$\begin{aligned}
\hat{\boldsymbol{A}}_\infty &= \begin{bmatrix}
-1.975\text{e}1 & 1 & -1.975\text{e}1 & 0 & -1.975\text{e}1 & 0 & 0 & 0 \\
-9.950\text{e}1 & -1.000\text{e}{-4} & -9.950\text{e}1 & 0 & -9.950\text{e}1 & 0 & 0 & 0 \\
2.751\text{e}0 & 0 & 2.751\text{e}0 & 1 & 2.751\text{e}0 & 0 & 0 & 0 \\
-4.448\text{e}1 & 0 & -4.073\text{e}2 & -1.458\text{e}0 & -4.061\text{e}1 & 4.209\text{e}0 & -2.816\text{e}{-5} & 0 \\
1.438\text{e}{-2} & 0 & 1.438\text{e}{-2} & 0 & 1.438\text{e}{-2} & 1 & 0 & 0 \\
-3.260\text{e}{-1} & 0 & 2.087\text{e}3 & 8.417\text{e}0 & -3.181\text{e}1 & -3.429\text{e}1 & 2.294\text{e}{-4} & 0 \\
-2.137\text{e}7 & 0 & -2.137\text{e}7 & 0 & -2.137\text{e}7 & -1.486\text{e}9 & 5.821\text{e}{-11} & 1.260\text{e}5 \\
-6.634\text{e}3 & -7.962\text{e}4 & 4.892\text{e}1 & 1.888\text{e}0 & -6.633\text{e}3 & 2.319\text{e}{-1} & -4.467\text{e}{-6} & -6.751\text{e}0
\end{bmatrix} \\
\hat{\boldsymbol{B}}_\infty^T &= \begin{bmatrix} 4.191\text{e}0 & 2.111\text{e}1 & -5.834\text{e}{-1} & 9.435\text{e}0 & -3.050\text{e}{-3} & 6.916\text{e}{-2} & 4.533\text{e}6 & 3.300\text{e}{-6} \end{bmatrix} \\
\hat{\boldsymbol{C}}_\infty &= \begin{bmatrix} -4.691\text{e}3 & -5.630\text{e}4 & 3.459\text{e}1 & 1.335\text{e}{-1} & -4.690\text{e}3 & 1.640\text{e}{-1} & -3.159\text{e}{-6} & -5.933\text{e}{-2} \end{bmatrix}
\end{aligned} \tag{3.21}$$

The resulting control scheme is presented in Fig. 3.4.

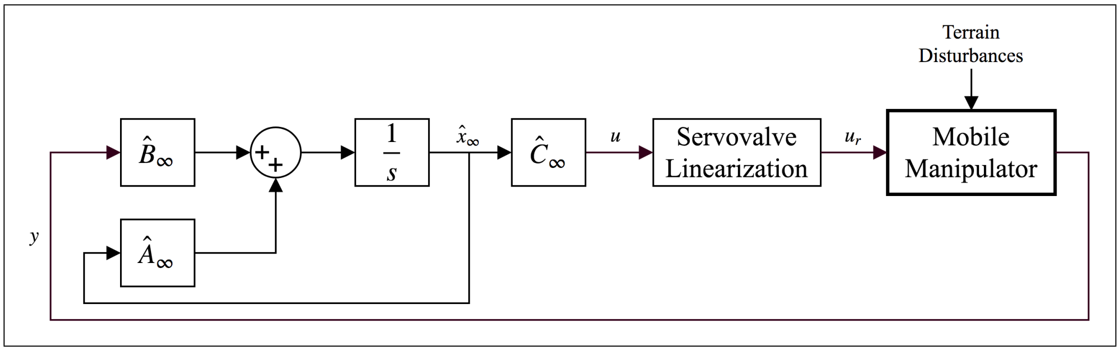

FIGURE 3.4. $\mathcal{H}_\infty$ control scheme.

The only tuning parameter involved is the manipulated variable weight D introduced in (3.17). This parameter is adjusted to $1 \cdot 10^{-4}$, such that the control input variable u_∞ operates within the machine's admissible limits. The resulting open and closed-loop responses of the first component of $\boldsymbol{z}_\infty$ to an input disturbance $a_{1,\theta}$, are presented in Fig. 3.5.

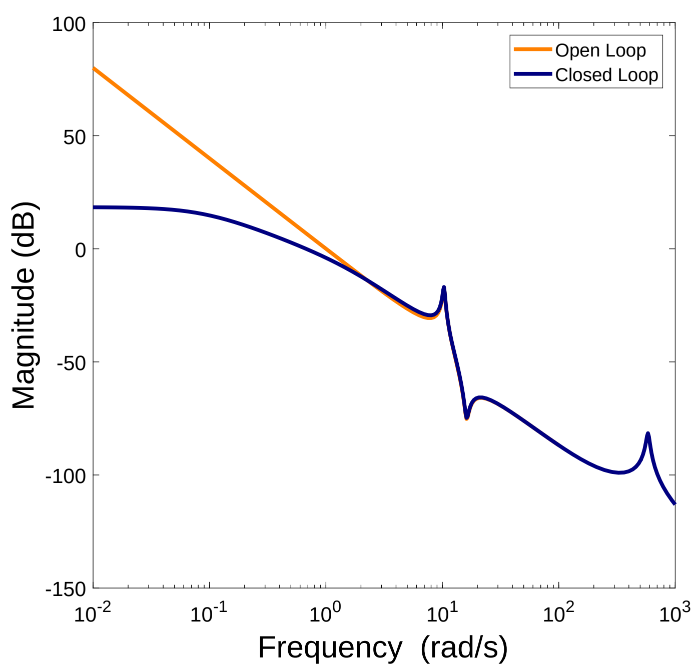

FIGURE 3.5. Open and closed-loop response of the first component of $\boldsymbol{z}_\infty$ to an input disturbance $a_{1,\theta}$.

3.2.4. Alternative $\mathcal{H}_\infty$ Control Design

An alternative $\mathcal{H}_\infty$ controller is designed, which considers the base pitch rate $\dot{\theta}$ as a measurement for computing the dynamic control law, instead of using it to compute a feedforward action as established for the proposed control strategy (3.1). In theory, this controller should provide an optimal solution when considering both measurements for feedback control. As presented in Chapter 5, it effectively has better performance than the $\mathcal{H}_\infty$ designed for the single-output system. It also tends to respond better to high frequency disturbances compared to the proposed structure with $\mathcal{H}_\infty$ and feedforward. Nonetheless, its low frequency performance is subpar, with steady-state errors, and performs poorly on real equipment as differences with the model used for design purposes become more evident, and this structure is highly dependent on an accurate model. For these reasons, this control structure is presented as a comparison to the proposed structure with feedforward.

The measured variables available to this alternative $\mathcal{H}_\infty$ controller are:

$$\boldsymbol{y} = \begin{bmatrix} x_2 \\ x_1 + x_3 + x_5 \end{bmatrix} = \begin{bmatrix} \dot{\theta} \\ \theta + q_1 + q_2 \end{bmatrix} \tag{3.22}$$

Similarly to the case of the single-output $\mathcal{H}_\infty$ controller, the output variable $x_1+x_3+x_5$ is computed directly from the inclinometer located on the bucket, which measures the bucket tilt angle with respect to the gravity vector. On the other hand, the base pitch rate $x_2 = \dot{\theta}$ is measured using an IMU. The disturbance $a_{1,\theta}$ produces changes in the pitch rate, i.e. the disturbance enters the system through $\dot{x}_2 \propto a_{1,\theta}$. For this case, the same performance output (3.17) is considered for the controller design.

As in the single-output case, additional disturbance inputs are defined, such that the condition for $\boldsymbol{D}_{21}\boldsymbol{D}_{21}^T$ being invertible is satisfied. These new disturbances correspond to the sensor noises, and their respective coefficients in matrix $\boldsymbol{D}_{21}$ are set in relation to the relative magnitude between the tilt and pitch rate sensor measurements and noise. The partitioned plant representation (3.5) used for control design of this alternative $\mathcal{H}_\infty$ controller which considers two system outputs is presented in (3.23).

$$
\boldsymbol{A} = \begin{bmatrix} 0 & 1 & 0 & 0 & 0 & 0 & 0 & 0 \\ -2.500\text{e}{-9} & -1.000\text{e}{-4} & 0 & 0 & 0 & 0 & 0 & 0 \\ 0 & 0 & 0 & 1 & 0 & 0 & 0 & 0 \\ 0 & 0 & -3.629\text{e}2 & -1.458\text{e}0 & 3.864\text{e}0 & 4.209\text{e}0 & -2.816\text{e}{-5} & 0 \\ 0 & 0 & 0 & 0 & 0 & 1 & 0 & 0 \\ 0 & 0 & 2.087\text{e}3 & 8.417\text{e}0 & -3.148\text{e}1 & -3.429\text{e}1 & 2.294\text{e}-4 & 0 \\ 0 & 0 & 0 & 0 & 0 & -1.486\text{e}9 & 0 & 1.260\text{e}5 \\ 0 & 0 & 0 & 0 & 0 & 0 & 0 & -6.667\text{e}0 \end{bmatrix}
$$

$$
\boldsymbol{B}_1 = \begin{bmatrix} 0 & 0 & 0 \\ 1 & 0 & 0 \\ 0 & 0 & 0 \\ -3.459\text{e}{-1} & 0 & 0 \\ 0 & 0 & 0 \\ -1.975\text{e}0 & 0 & 0 \\ 0 & 0 & 0 \\ 0 & 0 & 0 \end{bmatrix} \quad \boldsymbol{B}_2 = \begin{bmatrix} 0 \\ 0 \\ 0 \\ 0 \\ 0 \\ 0 \\ 0 \\ 6.667\text{e}0 \end{bmatrix}
$$

$$
\boldsymbol{C}_1 = \begin{bmatrix} 1 & 0 & 1 & 0 & 1 & 0 & 0 & 0 \\ 0 & 0 & 0 & 0 & 0 & 0 & 0 & 0 \end{bmatrix} \quad \boldsymbol{D}_{11} = \begin{bmatrix} 0 & 0 & 0 \\ 0 & 0 & 0 \end{bmatrix} \quad \boldsymbol{D}_{12} = \begin{bmatrix} 0 \\ D \end{bmatrix}
$$

$$
\boldsymbol{C}_2 = \begin{bmatrix} 0 & 1 & 0 & 0 & 0 & 0 & 0 & 0 \\ 1 & 0 & 1 & 0 & 1 & 0 & 0 & 0 \end{bmatrix} \quad \boldsymbol{D}_{21} = \begin{bmatrix} 0 & 1\text{e}{-3} & 0 \\ 0 & 0 & 1\text{e}{-2} \end{bmatrix} \quad \boldsymbol{D}_{22} = \begin{bmatrix} 0 \\ 0 \end{bmatrix} \tag{3.23}
$$

The $\mathcal{H}_\infty$ problem of finding a controller of the form $u_\infty^* = \boldsymbol{K} * \boldsymbol{y}$ that minimizes the closed-loop transfer matrix from disturbance input $a_{1,\theta}$ to the performance output $\boldsymbol{z}_\infty$ (3.19), is again solved using the two-Riccati formulae described in Section 3.2 and the standard γ-iteration technique based on the bisection algorithm implemented in (Balas et al., 2015). The resulting controller is implemented as a dynamical system:

$$
\begin{aligned}
\dot{\hat{\boldsymbol{x}}}_\infty^* &= \hat{\boldsymbol{A}}_\infty^* \hat{\boldsymbol{x}}_\infty^* + \hat{\boldsymbol{B}}_\infty^* \boldsymbol{y} \\
u_\infty^* &= \hat{\boldsymbol{C}}_\infty^* \hat{\boldsymbol{x}}_\infty^*
\end{aligned} \tag{3.24}
$$

with input $\boldsymbol{y}$, output u_∞^*, internal states $\hat{\boldsymbol{x}}_\infty^*$ and state-space matrices $\hat{\boldsymbol{A}}_\infty^*, \hat{\boldsymbol{B}}_\infty^*, \hat{\boldsymbol{C}}_\infty^*$ given in (3.25).

$$
\hat{\boldsymbol{A}}_{\infty}^{*} = \begin{bmatrix}
-7.043\text{e}{-2} & 7.259\text{e}{-4} & -7.043\text{e}{-2} & 0 & -7.043\text{e}{-2} & 0 & 0 & 0 \\
9.843\text{e}1 & -9.951\text{e}2 & 9.843\text{e}1 & 0 & 9.843\text{e}1 & 0 & 0 & 0 \\
-1.428\text{e}{-1} & 4.117\text{e}{-1} & -1.428\text{e}{-1} & 1 & -1.428\text{e}{-1} & 0 & 0 & 0 \\
-4.068\text{e}1 & 4.098\text{e}2 & -4.036\text{e}2 & -1.458\text{e}0 & -3.682\text{e}1 & 4.209\text{e}0 & -2.816\text{e}{-5} & 0 \\
-2.129\text{e}{-1} & 1.436\text{e}0 & -2.129\text{e}{-1} & 0 & -2.129\text{e}{-1} & 1 & 0 & 0 \\
-1.417\text{e}0 & 1.430\text{e}0 & 1.945\text{e}3 & 8.417\text{e}0 & -1.731\text{e}2 & -3.429\text{e}1 & 2.294\text{e}{-4} & 0 \\
2.120\text{e}8 & -2.135\text{e}9 & 2.120\text{e}8 & 0 & 2.120\text{e}8 & -1.486\text{e}9 & 5.821\text{e}{-11} & 1.260\text{e}5 \\
-5.963\text{e}3 & -7.952\text{e}4 & 3.942\text{e}1 & 1.528\text{e}0 & -5.962\text{e}3 & 1.876\text{e}{-1} & -4.015\text{e}{-6} & -6.742\text{e}0
\end{bmatrix}
$$

$$
\hat{\boldsymbol{B}}_{\infty}^{*T} = \begin{bmatrix}
4.331\text{e}{-1} & 4.313\text{e}2 & -1.784\text{e}{-1} & -1.776\text{e}2 & -6.225\text{e}{-1} & -6.197\text{e}2 & 9.255\text{e}8 & 7.061\text{e}{-5} \\
3.053\text{e}{-2} & -4.266\text{e}1 & 6.188\text{e}{-2} & 1.763\text{e}1 & 9.230\text{e}{-2} & 6.140\text{e}1 & -9.187\text{e}7 & 4.265\text{e}{-2}
\end{bmatrix}
$$

$$
\hat{\boldsymbol{C}}_{\infty}^{*} = \begin{bmatrix}
-2.064\text{e}3 & -2.752\text{e}4 & 1.368\text{e}1 & 5.290\text{e}{-1} & -2.063\text{e}3 & 6.498\text{e}{-2} & -1.389\text{e}{-6} & -2..612\text{e}{-2}
\end{bmatrix}
\tag{3.25}
$$

The resulting control scheme is presented in Fig. 3.6.

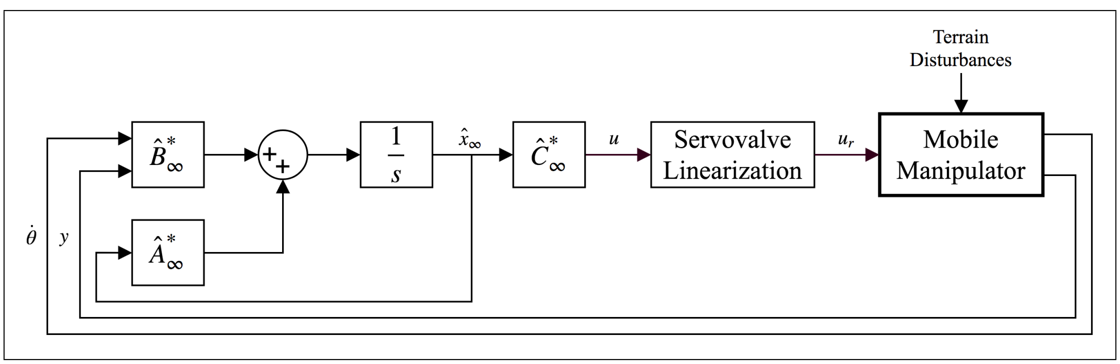

FIGURE 3.6. Alternative $\mathcal{H}_{\infty}$ control scheme.

It is noted that the only tuning parameter involved is again the manipulated variable weight D introduced in (3.17). In this case, the parameter is adjusted to $5 \cdot 10^{-4}$, such that the control input variable u_{∞}^{*} operates within the machine's admissible limits. The resulting open and closed-loop responses of the first component of $\boldsymbol{z}_{\infty}$ to an input disturbance $a_{1,\theta}$, are presented in Fig. 3.7.

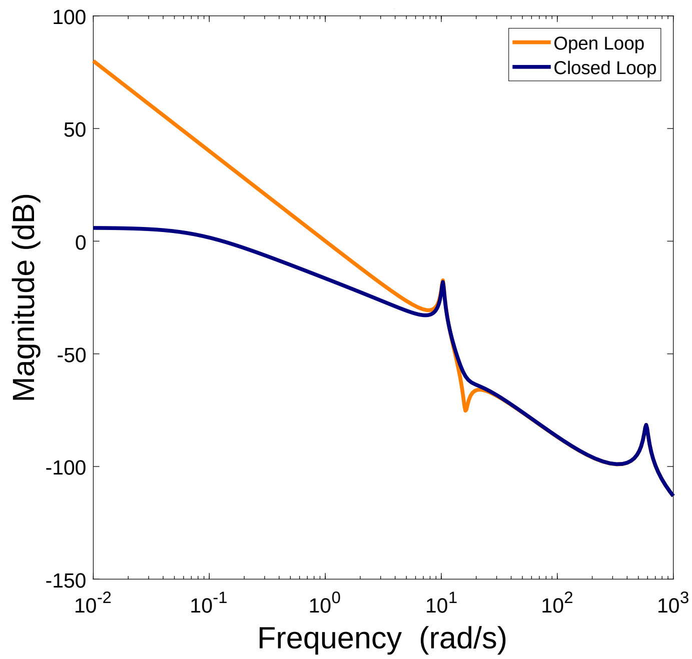

FIGURE 3.7. Open and closed-loop response of the first component of $\boldsymbol{z}_\infty$ to an input disturbance $a_{1,\theta}$.

3.3. Mobile Base Pitch Rate Feedforward

Changes in slope of the terrain can be estimated from the pitch rate $\dot{\theta}$ using inertial measurements. Considering a linear input-output gain K_u of the hydraulic actuators, the effect of pitch rate of the mobile base can be reduced by direct feedforward of the form:

$$u_{ff}(t) = -K_u^{-1}\dot{\theta}(t) = K_{ff}\dot{\theta}(t) \tag{3.26}$$

This feedforward action will not be able to completely cancel the effect of the mobile base pitch rate on the end-effector tilt, due to the time constant present in the hydraulic actuators which limits the feedforward action bandwidth, but it should be effective in reducing tilt variations induced by the terrain profile traversed by the mobile manipulator, especially when traveling at low speeds.

In the case of the proposed terrain disturbance rejection approach combining $\mathcal{H}_\infty$ control (3.20) with feedforward (3.26), the resulting control law is:

$$\begin{aligned} \dot{\hat{\boldsymbol{x}}}_\infty &= \hat{\boldsymbol{A}}_\infty \hat{\boldsymbol{x}}_\infty + \hat{\boldsymbol{B}}_\infty y \\ u = u_\infty + u_{ff} &= \hat{\boldsymbol{C}}_\infty \hat{\boldsymbol{x}}_\infty + K_{ff}\dot{\theta} \end{aligned} \tag{3.27}$$

and the resulting control scheme is presented in Fig. 3.8.

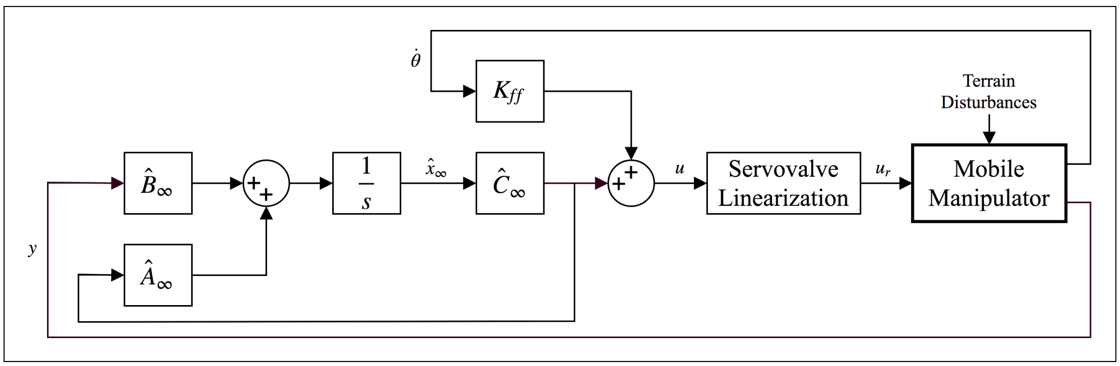

FIGURE 3.8. Proposed $\mathcal{H}_\infty$ + feedforward control scheme.

Whereas for the comparison scheme combining ADRC with feedforward, the control law is computed by summing the outputs from controllers (3.4) and (3.26), which results in:

$$u = u_{ADRC} + u_{ff} = \frac{1}{b}\left(-bK_p y + -\frac{bK_d}{sT_f+1}\dot{y} - \hat{\zeta}_3\right) + K_{ff}\dot{\theta} \tag{3.28}$$

and the resulting comparison control scheme is presented in Fig. 3.9.

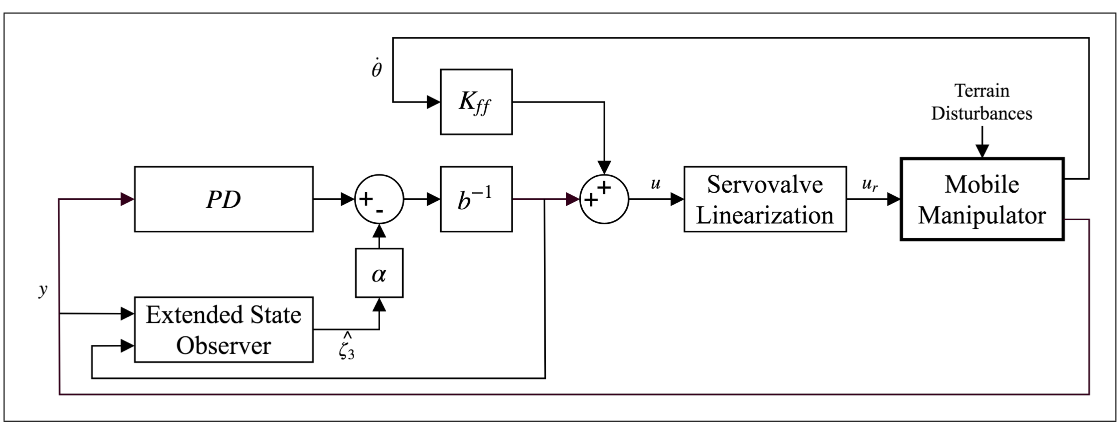

FIGURE 3.9. ADRC + feedforward control scheme.

The effect of feedforward in the closed-loop response of the first component of $\boldsymbol{z}_\infty$ to an input disturbance $a_{1,\theta}$ is presented in 3.10. It is evident that the introduction of feedforward aids in the reduction of the low frequency component of terrain disturbances.

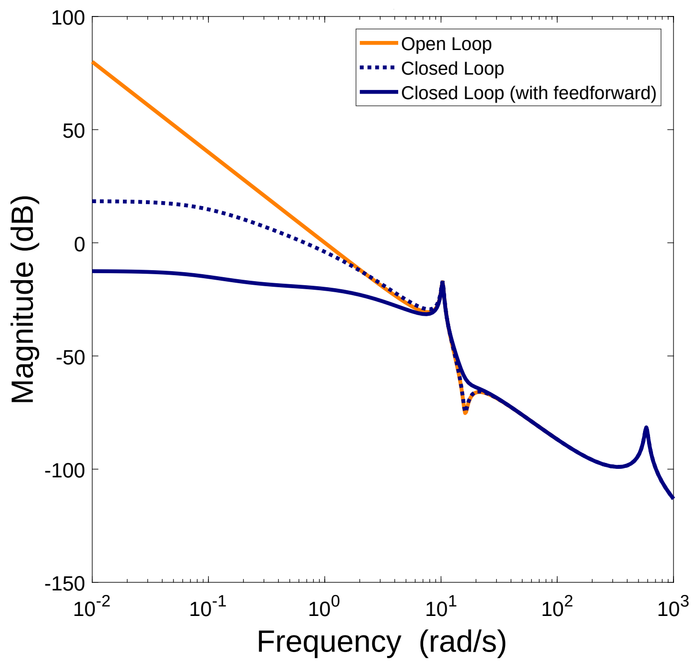

FIGURE 3.10. Open and closed-loop response of the first component of z_∞ to an input disturbance $a_{1,\theta}$, considering mobile base pitch rate feedforward.

3.4. Servovalve Input-Output Linearization

The open-loop response of the bucket's tilt to the servovalve's input signal is highly nonlinear as explained in Section 2. In fact, the bucket's tilt rate responds to different values of the servovalve's input signal, the duty cycle of a pulse-width modulated signal, with a noticeable dead zone and a quadratic behavior in the active region as shown in Fig. 3.11. If $\phi : u_r \rightarrow \dot{y}$ denotes a static nonlinear relation between the tilt rate $\dot{y}$ and servovalve's input u_r, i.e. $\dot{y} = \phi(u_r)$, a transformation $g \overset{def}{=} \phi^{-1} : u \rightarrow g(u)$, applied to signal u allows to render the tilt rate linear with respect to the controller's output, i.e. $\dot{y} = \phi(u_r)$ with $u_r = g(u)$, implies $\dot{y} = \phi(g(u)) = \phi(\phi^{-1}(u)) = u$. Considering the experimentally measured servovalve's response shown in Fig. 3.11, an inverse function:

$$u_r = g(u) \stackrel{def}{=} \begin{cases} -\alpha_1(-u)^{1/2} - \beta_1 & u < 0 \\ \alpha_2 u^{1/2} + \beta_2 & u \geq 0 \end{cases} \tag{3.29}$$

is computed based on a quadratic fitting of the registered actuator's response data to compute the parameters α_1, β_1, α_2, β_2, and thus provide a linearizing transformation of the servovalve's input-output relation. The resulting linear input-output response obtained from experimental measurements is presented in Fig. 3.11. The input-output gain relating the input to the joint angular velocity is defined as K_u and used to compute the feedforward action presented in (3.26).

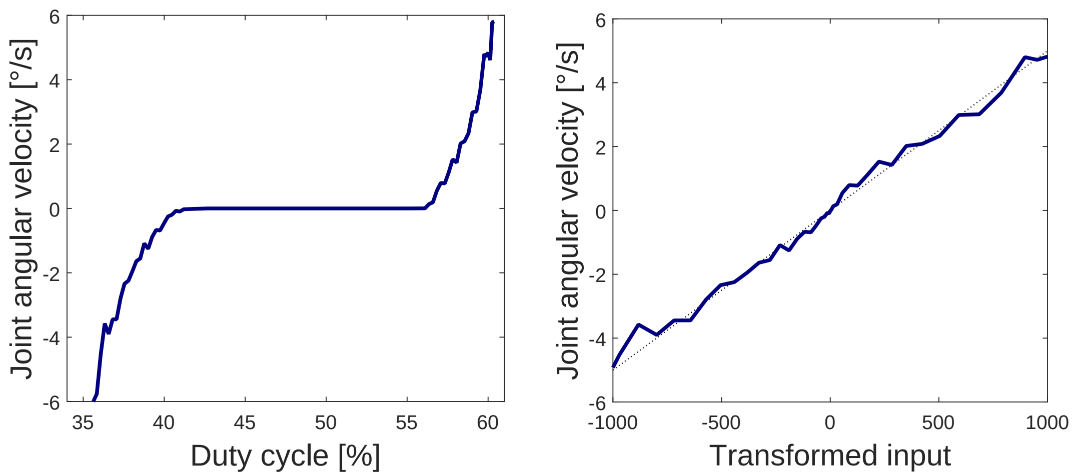

FIGURE 3.11. Steady state bucket joint angular velocity for servovalve raw duty cycle and transformed input.

4. SIMULATIONS AND EXPERIMENTAL SETUP

4.1. Simulation Setup

The proposed controller is first evaluated on a simulated skid-steer mobile manipulator (Fig. 4.1) available in (Aguilera-Marinovic & Torres-Torriti, 2014). The simulation files are based on Featherstone's Spatial Software (Featherstone, 2012) for Matlab® and Simulink®. The Spatial Software provides a set of tools for constructing dynamic models of non-ground constrained articulated bodies using spatial vector algebra. It is also possible to set contact points for the system's ground interactions, and simulate the respective forces applied upon contact. The Spatial Software also provides functions for visualizing the results, both as data graphs or 3D animations of the simulated system.

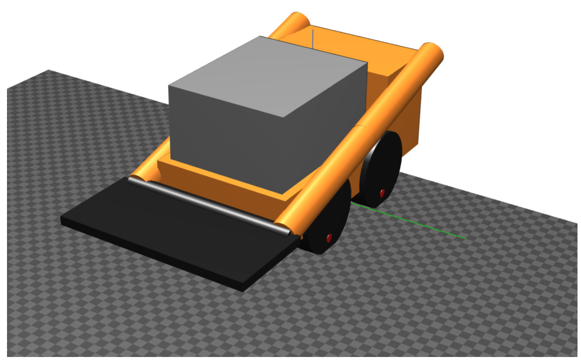

FIGURE 4.1. Simulated skid-steer loader.

The skid-steer mobile manipulator model used for simulations integrates the dynamic equations and wheel-ground interactions discussed in Chapter 2. Equations for the torque applied by the wheel motors, joint friction torques and ground contact points are also included. The accuracy of this model was validated in (Aguilera-Marinovic et al., 2017). The available model was updated through the inclusion of the equations of the system's hydraulic actuators and dampened spring-like forces discussed in Chapter 2. Discrete realizations with a sampling time of 2 ms of the controllers described in Chapter 3 were also added to the existing model. The model parameters used for simulations are presented in Table 3.1.

The simulation structure is presented in Fig. 4.2. Vector $\mathbf{x}_1$ corresponds to the mobile base spatial positions and velocities, and vector q corresponds to the joint positions. Joint torques are included in the term τ_i. Lastly, F_{ext} represents all external forces, such as the wheel-ground interaction forces acting on contact points with the ground.

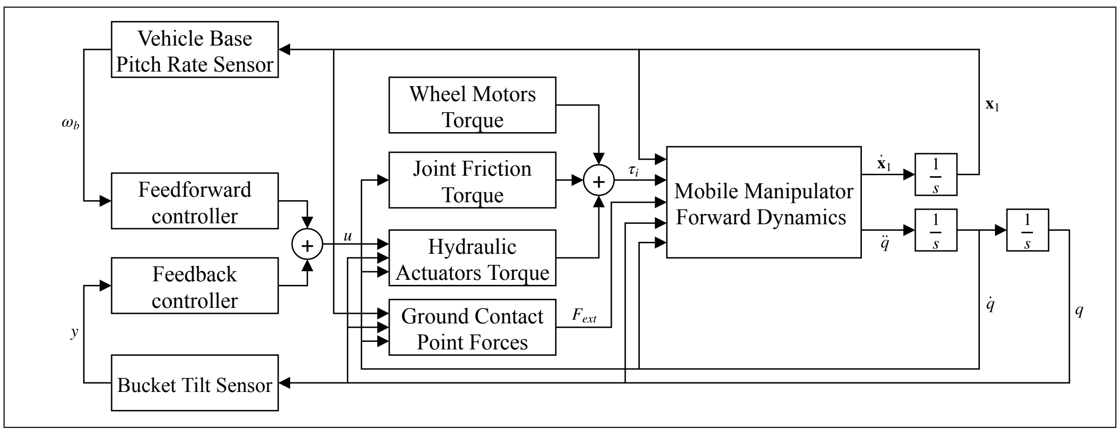

FIGURE 4.2. Simulation structure.

4.2. Experimental Setup

The simulation results are experimentally validated using an industrial compact skid-steer loader Cat®262C shown in Fig. 4.3. The automation of the loader has been developed over the last years by the Robotics and Automation Laboratory at PUC. The semi-autonomous loader is equipped with tilt sensors, IMUs, a navigation computer and wireless communication interfaces to make it semi-autonomous. The loader is also equipped with other sensors not used in this work, such as wheel encoders, lidars and GPS.

The manipulator end effect orientation was measured using a TE connectivity MEAS inclinometer positioned on the bucket joint. This sensor's typical applications include tool leveling for off-road vehicles. For the base tilt rate measurement, two Vectornav VN-200 IMUs were used. The IMUs are positioned one at each side of the vehicle base, such that base tilt rate is computed from the mean value of the measurements from both sensors.

FIGURE 4.3. Industrial Cat®262C loader.

In order to acquire data from the sensors and actuate the machine's manipulator more smoothly, the C language software of the Masterboard installed on the semi-autonomous loader was updated. The control software developed on the C++ language is executed on an external PC connected to the Masterboard. Control inputs for the hydraulic actuators are sent to the Masterboard in the form of 12-bit encoded duty cycles, at a rate of 2ms. In turn, the Masterboard responds with measurements from the sensors. The control software can cycle between the different feedback controllers, such as PD, ADRC and $\mathcal{H}_\infty$ control, as well as toggle the feedfoward action based on vehicle base pitch rate measurements.

4.3. Discrepancies Between Simulations and Real Equipment

The industrial skid-steer loader used for experiments presents some important discrepancies with the described model, which worsen the terrain disturbance rejection on real equipment compared to simulations. These factors are difficult to model, since they are complex to accurately represent through dynamic equations and the related parameters are very difficult to measure accurately in practice. Some of these factors are approximated through simplified equations, while others are left entirely unmodeled and thus treated as a disturbance. The two factors which have the greatest impact and are not adequately considered in the simulated model are briefly illustrated in the following sections.

4.3.1. Manipulator Non-Rigidity

The model used to represent the mobile manipulator dynamics considers the arm links as rigid bodies, but in practice, this is not the case. As observed from Fig. 4.4, when traversing different terrain profiles with no control input, the end-effector bucket tilt does not precisely follow the vehicle base pitch. Instead, it oscillates around the vehicle base pitch, mildly in the case of a ramp, but in a pronounced manner when driving over a road bump, more so at a higher speed. This oscillatory behavior is somewhat considered by the model equations, through the spring-like forces introduced on the manipulator arm link, though not to the extent at which it occurs in practice.

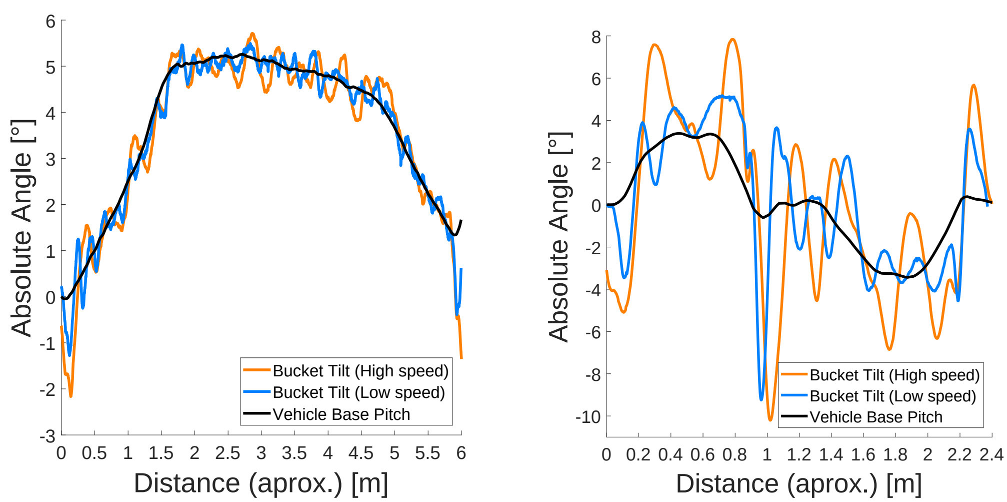

(A) End effector oscillations when traversing a ramp.

(B) End effector oscillations when traversing a road bump.

FIGURE 4.4. End effector oscillations due to manipulator non-rigidity.

4.3.2. Actuator Recoil

A sudden change in the input signal fed to the hydraulic actuators generates a recoil in the manipulator bucket tilt, characteristic of a non-minimum phase system. The actuator recoil becomes more notorious as the immediate change in the input variable increases, as evidenced by Fig. 4.5.

This effect results in noticeable overshoot and oscillation of the response that worsens control performance and may even destabilize the closed loop system. For this reason,

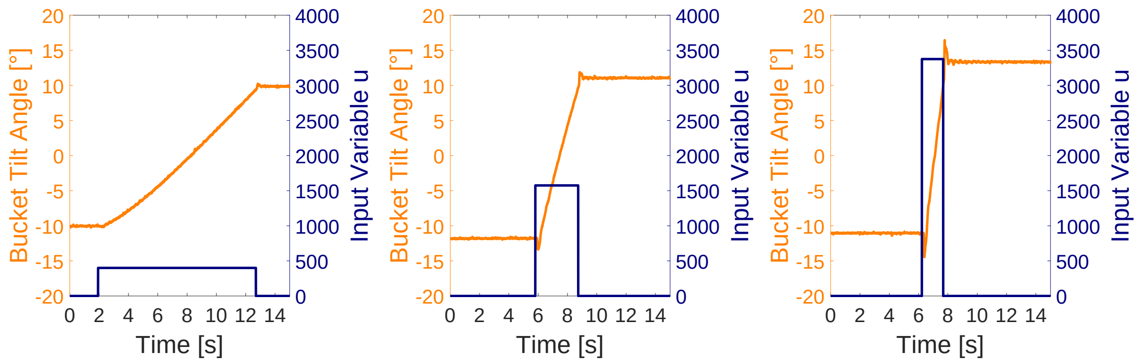

FIGURE 4.5. Bucket tilt recoil towards different inputs u.

the manipulated variable is artificially saturated such that $|u| \leq 1000$. As a consequence, control performance becomes significantly limited, especially at higher frequencies, since the controller is unable to respond sufficiently fast to disturbances which introduce high rate changes in the bucket tilt.

4.4. Test Methodology

The experiments were carried out driving the mobile robotic manipulator over a 4 m long, 30 cm high ramp and a 10 cm high, 60 cm long road bump at low and high speeds, respectively corresponding to 12.5% and 25% of the maximum vehicle speed of 12.5 km/h. These experiments were chosen to study the system's response to different ground normal forces resulting in low and high frequency disturbances. For the ramp experiments, the bucket's inclination is measured from the initial contact of the front wheel with the ramp until the rear wheel exits the ramp. In the bump experiments, the bucket's inclination is measured from initial contact of the front wheel with the bump until oscillations cease after the rear wheel has rolled over the bump. The instants at which the front and rear wheels reach the peak of the bump are indicated respectively by t_1 and t_2 on Figs. 5.3, 5.4, 5.5, 5.6, 5.9 and 5.10.

Additional control schemes were evaluated as comparison benchmarks. These include both ADRC and $\mathcal{H}_\infty$ without feedforward and a standard PD with the same gains as those used for the ADRC scheme. All control schemes are sampled at 2 ms.

The results are also compared to the measured motion without any ground disturbance attenuation strategy. The root-mean square error:

$$\text{RMSE} = \sqrt{\frac{1}{T}\int_0^T (r(t) - y(t))^2 \, dt} \tag{4.1}$$

is computed for a reference inclination $r(t) = 0$, considering the entire experiment time duration T for each control scheme. Each test is repeated three times on the real mobile manipulator in order to compute the mean RMS error for each scheme.

5. RESULTS

5.1. Simulation Results

5.1.1. Ramp Simulations

The results for simulations driving the robotic loader over a ramp are presented in Figs. 5.1 and 5.2, and summarized in Table 5.1. It is observed that all control schemes are successful in reducing the RMSE metric. The proposed scheme incorporating $\mathcal{H}_\infty$ control and feedforward is able to maintain an almost level bucket throughout the entire course of the ramp, and presents disturbance reductions of nearly 98% at low speed and 95% at high speed. In comparison, both the ADRC with feedforward and alternative $\mathcal{H}_\infty$ have slightly worse performance metrics than the proposed scheme. When feedforward action is not included, error metric reductions for both speeds decrease approximately by 5-10% in the case of $\mathcal{H}_\infty$ control and 10-25% in the case of ADRC. The standard PD control presents worse performance than the other schemes, with reductions of 79% and 63% at low and high speed.

TABLE 5.1. End-effector angular error metrics (in degrees) for simulations over ramp.

	Low speed		High speed	
Control scheme	RMSE	Reduction	RMSE	Reduction
No control	3.64	—	3.58	—
PD	0.78	78.6%	1.34	62.6%
ADRC	0.62	83.0%	1.18	67.0%
$\mathcal{H}_\infty$	0.28	92.3%	0.64	82.1%
$\mathcal{H}_\infty$ (alternative)	0.35	90.4%	0.21	94.1%
ADRC + feedforward	0.23	93.7%	0.25	93.0%
$\mathcal{H}_\infty$ + feedforward	0.09	97.5%	0.18	95.0%

5.1.2. Road Bump Simulations

The results for simulations driving the robotic loader over a road bump are presented in Figs. 5.3 and 5.4, and summarized in Table 5.2. The proposed scheme presents RMSE metric reductions of 65% and 19% for the different speeds. In comparison, ADRC with feedforward presents almost the same performance with disturbance RMSE metric reductions of 61% and 19%. The alternative $\mathcal{H}_\infty$ control, on the other hand, presents worse performance than ADRC with feedforward at low speed, but presents the best performance at high speed with a RMSE metric reduction of 32%. When feedforward action is not included, error metric reductions for both speeds decrease approximately by 10-20% in the case of $\mathcal{H}_\infty$ control and 10-30% in the case of ADRC. The PD control presents a metric reduction of 33% at low speed, while at high speed error metric reduction is of 6%. It is noted though that the artificial actuator saturation imposed in Chapter 4 for the real equipment is also applied to the simulated loader for consistency, and this saturation becomes active on the road bump experiments, with the $\mathcal{H}_\infty$ controller being the most affected.

TABLE 5.2. End-effector angular error metrics (in degrees) for simulations over road bump.

	Low speed		High speed	
Control scheme	RMSE	Reduction	RMSE	Reduction
No control	2.88	—	3.04	—
PD	1.94	32.6%	2.85	6.3%
ADRC	1.87	35.1%	2.70	11.2%
$\mathcal{H}_\infty$	1.48	48.6%	2.69	11.5%
$\mathcal{H}_\infty$ (alternative)	1.29	55.2%	2.07	31.9%
ADRC + feedforward	1.12	61.1%	2.45	19.4%
$\mathcal{H}_\infty$ + feedforward	1.00	65.3%	2.45	19.4%

5.1.3. Road Bump Simulations (with Bucket Load)

In its mining application the studied front-end loader will usually have a loaded bucket, and as mentioned, the motivation behind this work is to reduce the spillage of carried material. The ideal approach would be to design an independent controller for the case of a loaded bucket, following the same procedure described in Chapter 3. This requires substitution of the respective parameters into the state-space representation and solving the resulting $\mathcal{H}_\infty$ optimal control problem. Nonetheless, to further test the proposed solution, simulations are carried out driving the robotic loader over the mentioned road bump while carrying a nominal bucket load of 1000 kg.

It must be noted that in practice, loading the bucket will modify the servovalve non-linear input-output response presented in Fig. 3.11, and thus, the currently applied transformation function will not result in a linearized servovalve input-output relation. To fix this issue, a different transformation function must be computed for the loaded bucket case.

The results for simulations driving the robotic loader with bucket load over a road bump are presented in Figs. 5.5 and 5.6, and summarized in Table 5.3. The proposed scheme presents RMSE metric reductions of 70% and 21% for the different speeds. The ADRC with feedforward presents slightly worse performance at low speed, with a disturbance RMSE metric reduction of 65%, but performs better at high speed with a metric reduction of 24%. The alternative $\mathcal{H}_\infty$ control performs worse at low speed but better at high speed with disturbance RMSE metric reductions of 63% and 37%. These metric reductions may appear better than those obtained during simulations without load, but the results of both tests are not comparable, since the trajectory followed by the manipulator changes due to the additional carried load. When feedforward action is not included, error metric reductions for both speeds decrease significantly: approximately by 15-20% in both cases. The PD control presents a metric reduction of 36% at low speed, while at high speed error metric reduction is 6%. Thus, it is concluded from simulations that the proposed approach is also effective for reducing the effect of terrain disturbances when the bucket is loaded but to a lesser extent, while the ADRC control is more robust to the changes in the system's dynamics introduced by the additional bucket load.

5.2. Experimental Results

5.2.1. Ramp Experiments

The results for experiments driving the robotic loader over a road bump are presented in Figs. 5.7 and 5.8, and summarized in Table 5.4. The proposed scheme incorporating $\mathcal{H}_\infty$ control and feedforward is able to maintain an almost level bucket throughout the entire course of the ramp at low speed with a disturbance reduction of 86%, and is able to

TABLE 5.3. End-effector angular error metrics (in degrees) for simulations over road bump (with bucket load).

	Low speed		High speed	
Control scheme	RMSE	Reduction	RMSE	Reduction
No control	2.79	—	2.87	—
PD	1.79	35.8%	2.70	5.9%
ADRC	1.57	43.7%	2.61	9.1%
$\mathcal{H}_\infty$	1.32	52.7%	2.68	6.6%
$\mathcal{H}_\infty$ (alternative)	1.02	63.4%	1.81	36.9%
ADRC + feedforward	0.99	64.5%	2.18	24.0%
$\mathcal{H}_\infty$ + feedforward	0.85	69.5%	2.26	21.3%

significantly reduce the effect of disturbances by 74% at high speed. In comparison, the ADRC with feedforward has slightly worse performance metrics of 83% and 68% at both speeds. When feedforward action is not included, error metric reductions for both speeds decrease approximately by 15-25% in the case of $\mathcal{H}_\infty$ control and 20% in the case of ADRC. In this experiment, the alternative $\mathcal{H}_\infty$ is outperformed even by the single-output $\mathcal{H}_\infty$ control without feedforward, as it significantly overcompensates when countering the effect of the base pitch rate on the bucket tilt when climbing the ramp. The standard PD control presents worse performance than the other schemes with metric reductions of 61% and 39% at low and high speed.

TABLE 5.4. End-effector angular error metrics (in degrees) for experiments over ramp.

	Low speed		High speed	
Control scheme	RMSE	Reduction	RMSE	Reduction
No control	3.65 ± 0.13	—	3.43 ± 0.05	—
PD	1.42 ± 0.08	61.1%	2.11 ± 0.04	38.5%
ADRC	1.39 ± 0.05	61.9%	1.81 ± 0.06	47.2%
$\mathcal{H}_\infty$	0.66 ± 0.01	81.9%	1.33 ± 0.02	61.2%
$\mathcal{H}_\infty$ (alternative)	1.07 ± 0.06	70.7%	1.39 ± 0.08	59.5%
ADRC + feedforward	0.62 ± 0.08	83.0%	1.11 ± 0.03	67.6%
$\mathcal{H}_\infty$ + feedforward	0.51 ± 0.02	86.0%	0.90 ± 0.10	73.8%

5.2.2. Road Bump Experiments

The results for experiments driving the robotic loader over a road bump are presented in Figs. 5.9 and 5.10, and summarized in Table 5.5. The proposed scheme presents RMSE

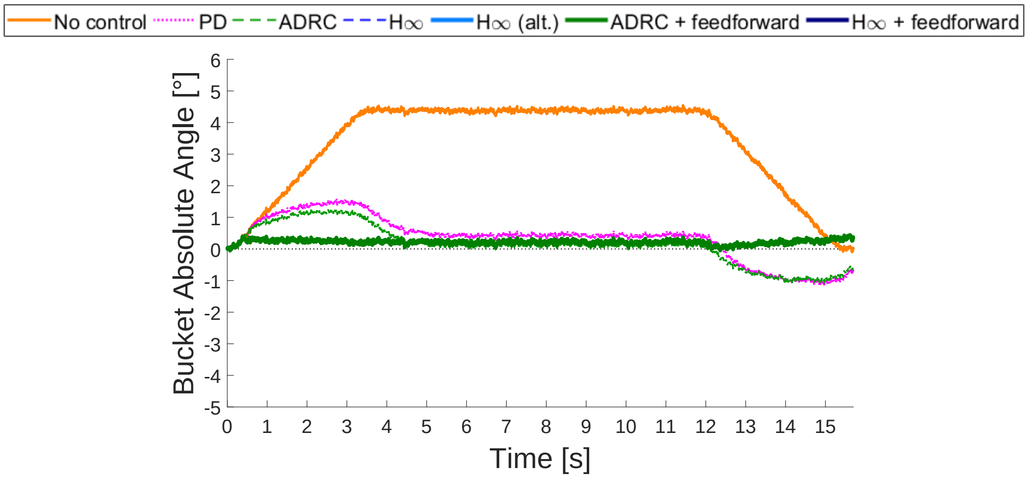

(A) ADRC.

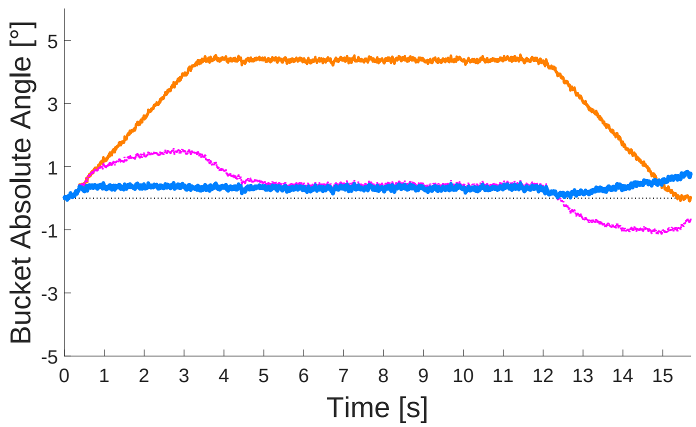

(B) Alternate $\mathcal{H}_\infty$ control.

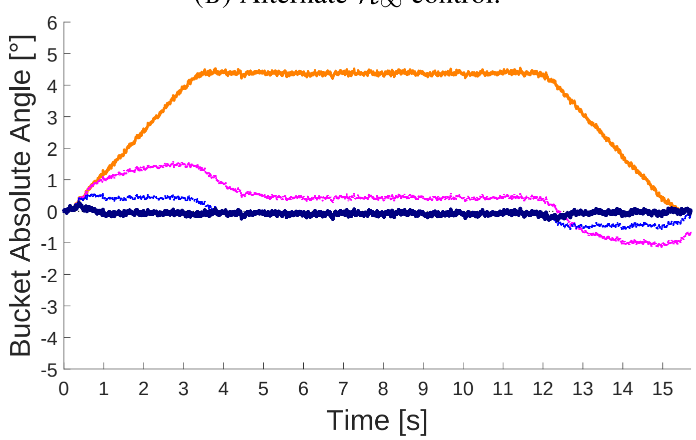

(C) $\mathcal{H}_\infty$ control.

FIGURE 5.1. Simulation results driving the robotic loader over a ramp at low speed.

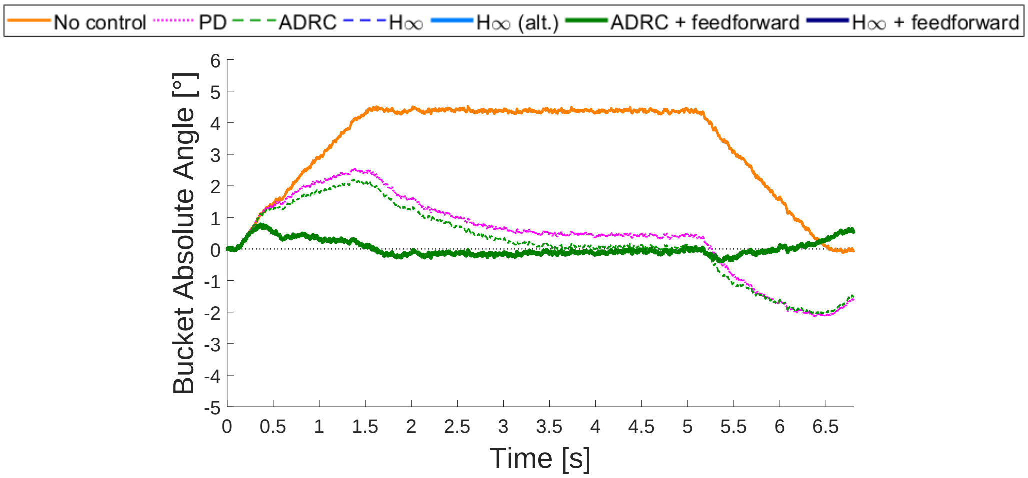

(A) ADRC.

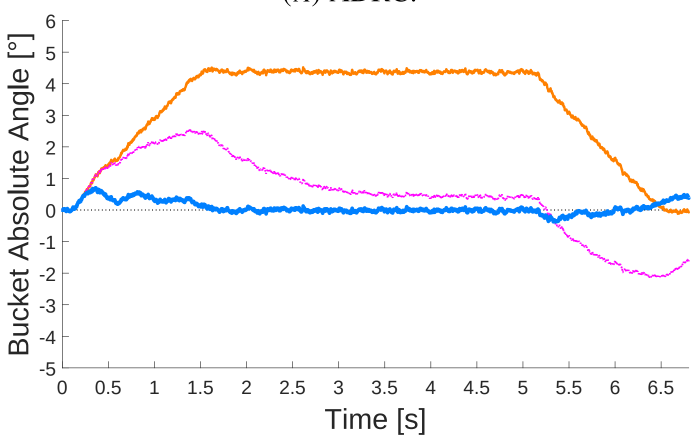

(B) Alternate $\mathcal{H}_\infty$ control.

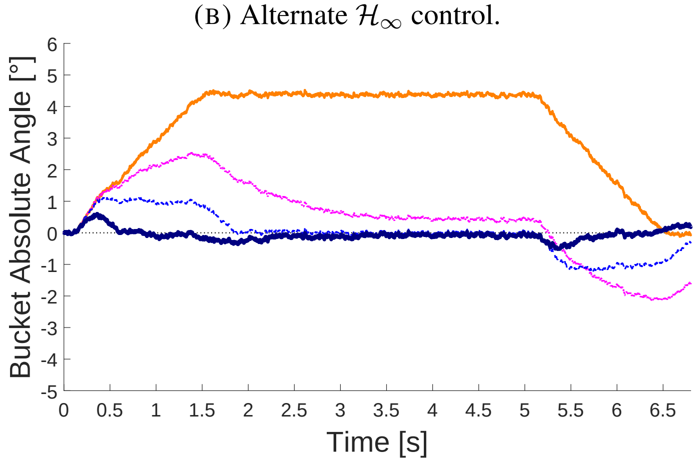

(C) $\mathcal{H}_\infty$ control.

FIGURE 5.2. Simulation results driving the robotic loader over a ramp at high speed.

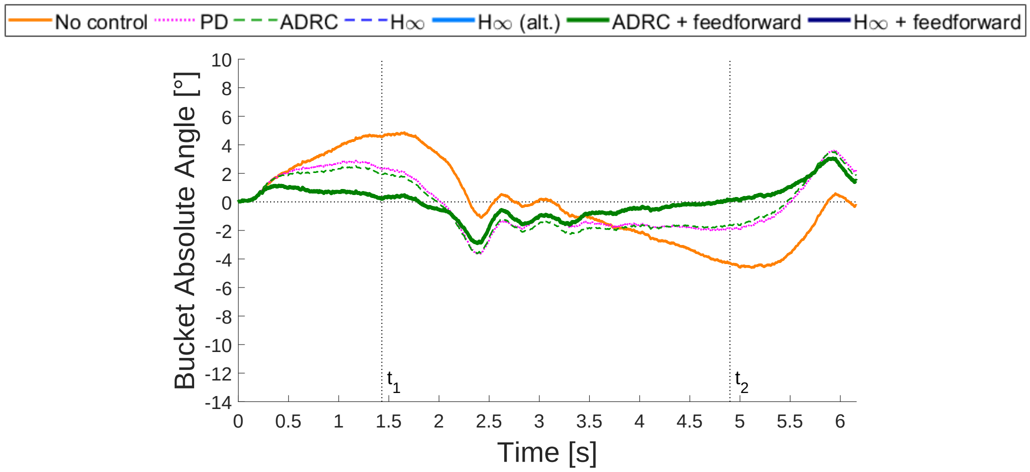

(A) ADRC.

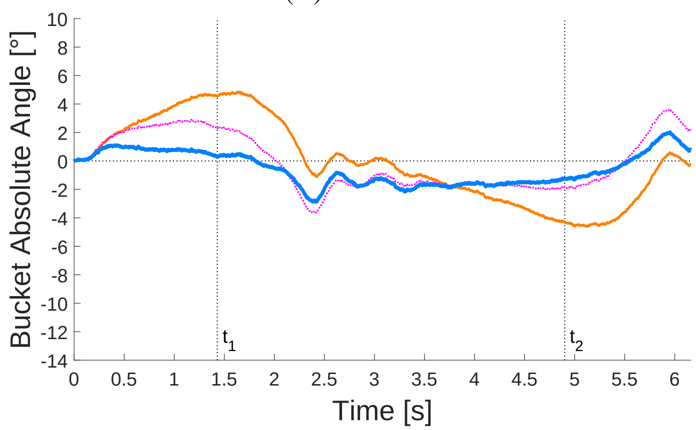

(B) Alternate $\mathcal{H}_\infty$ control.

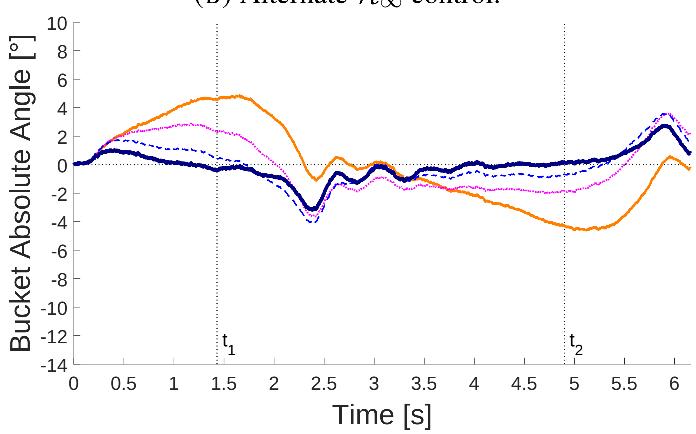

(C) $\mathcal{H}_\infty$ control.

FIGURE 5.3. Simulation results driving the robotic loader over a road bump at low speed.

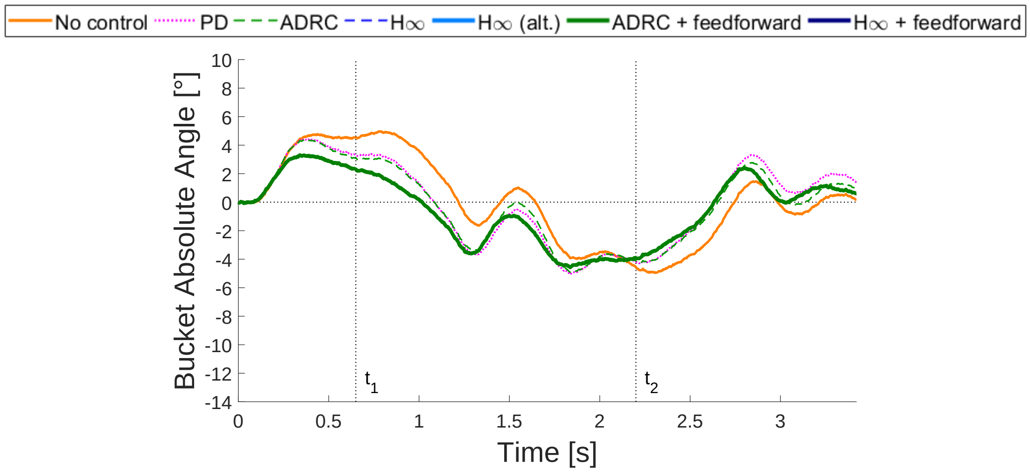

(A) ADRC.

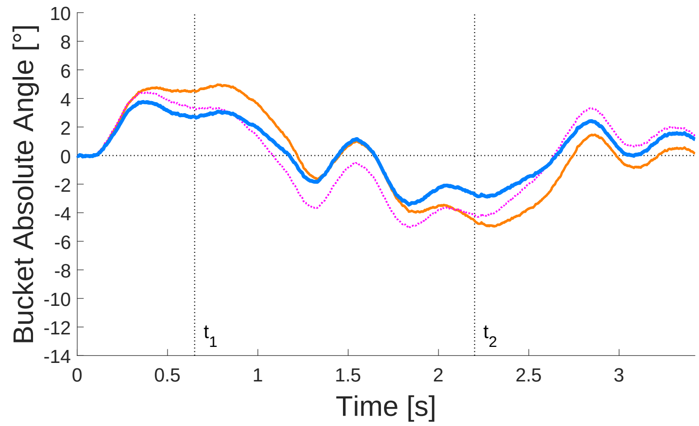

(B) Alternate $\mathcal{H}_\infty$ control.

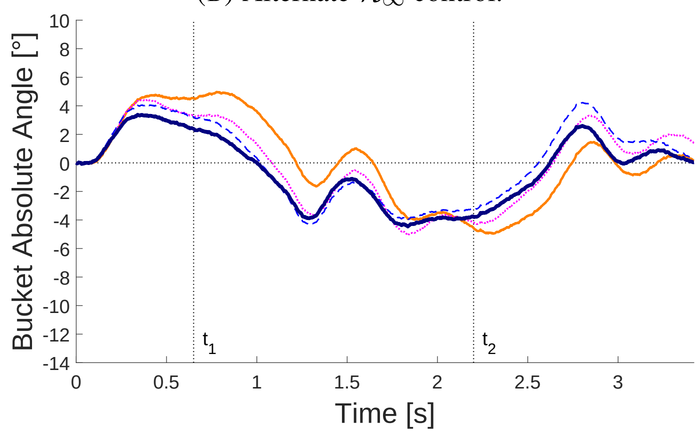

(C) $\mathcal{H}_\infty$ control.

FIGURE 5.4. Simulation results driving the robotic loader over a road bump at high speed.

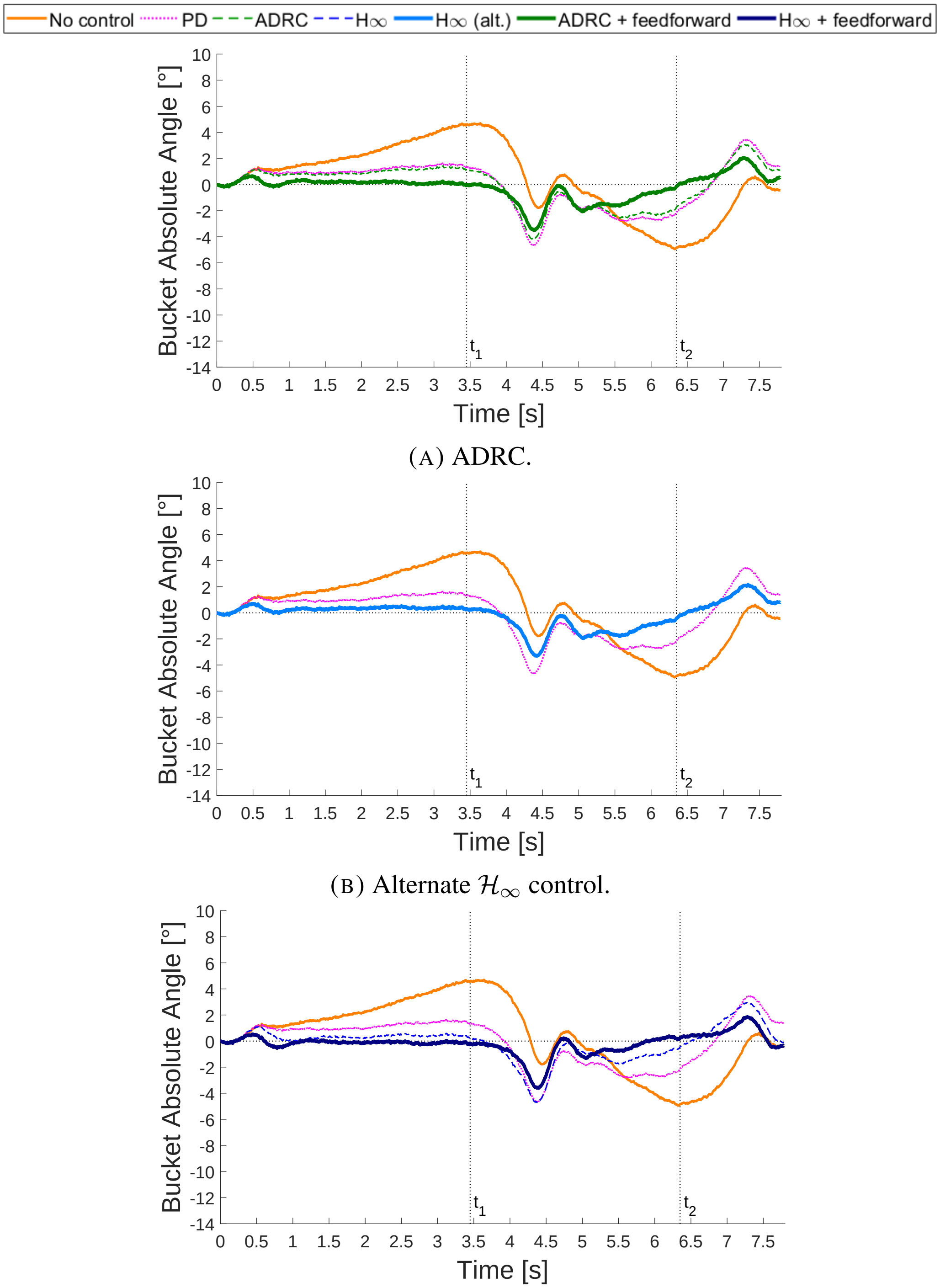

(A) ADRC.

(B) Alternate $\mathcal{H}_\infty$ control.

(C) $\mathcal{H}_\infty$ control.

FIGURE 5.5. Simulation results driving the robotic loader over a road bump at low speed (with bucket load).

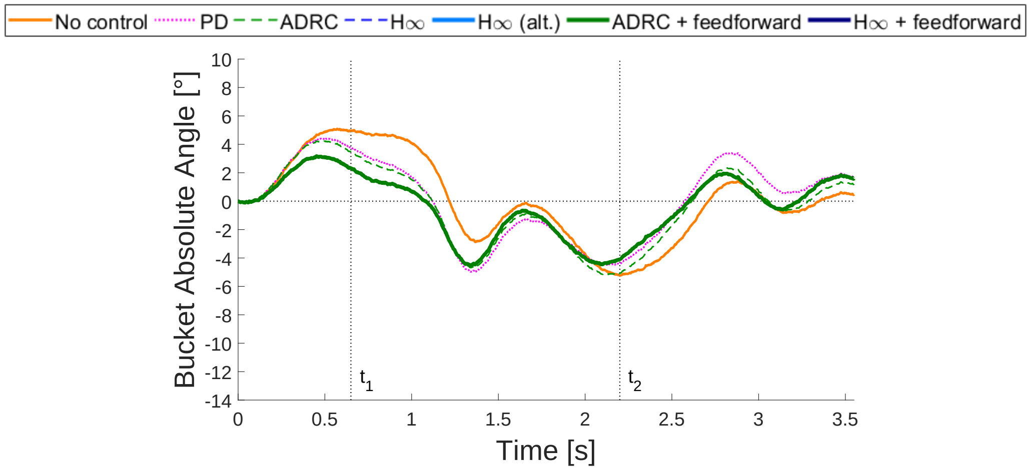

(A) ADRC.

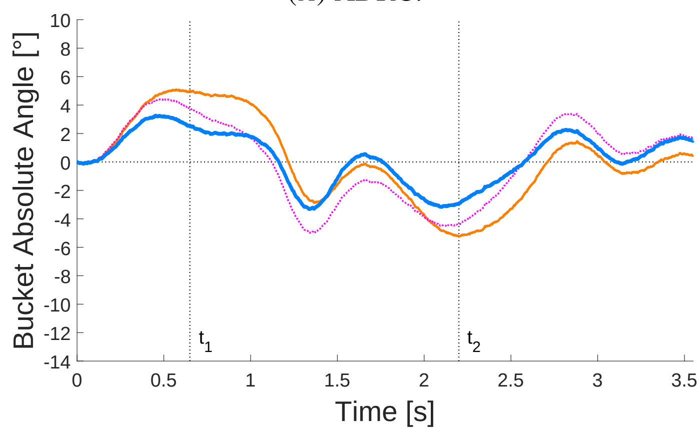

(B) Alternate $\mathcal{H}_\infty$ control.

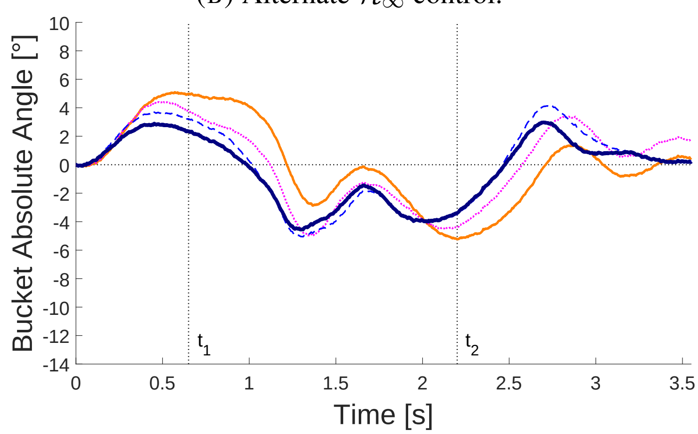

(C) $\mathcal{H}_\infty$ control.

FIGURE 5.6. Simulation results driving the robotic loader over a road bump at high speed (with bucket load).

metric reductions of 38% and 24% for the different speeds. The alternative $\mathcal{H}_\infty$ control scheme slightly underperforms at low speed with a metric reduction of 37% but presents the best results at high speed with a metric reduction of 27% at high speed. In comparison, ADRC with feedforward presents disturbance RMSE metric reductions of 30% and 10%, but with high oscillation around the level reference, particularly for the low speed case. This may be due to the aggressiveness of ADRC towards responses that differ considerably from its simplified second order dynamic system. When feedforward action is not included, error metric reductions for both speeds decrease approximately by 5-20% in the case of $\mathcal{H}_\infty$ control, whereas for ADRC the error metric reduction is reduced by approximately 20% at low speed but is almost the same at high speed. The PD control presents a metric reduction of 9% low speed, whereas at high speed the reduction is even less at only 3% at high speed with high overshoot.

TABLE 5.5. End-effector angular error metrics (in degrees) for experiments over road bump.

	Low speed		High speed	
Control scheme	RMSE	Reduction	RMSE	Reduction
No control	3.18 ± 0.09	—	4.43 ± 0.10	—
PD	2.88 ± 0.15	9.4%	4.30 ± 0.07	2.9%
ADRC	2.81 ± 0.09	11.6%	3.98 ± 0.23	10.2%
$\mathcal{H}_\infty$	2.62 ± 0.01	17.6%	3.66 ± 0.10	17.4%
$\mathcal{H}_\infty$ (alternative)	1.99 ± 0.05	37.4%	3.22 ± 0.04	27.3%
ADRC + feedforward	2.22 ± 0.02	30.2%	3.97 ± 0.05	10.4%
$\mathcal{H}_\infty$ + feedforward	1.96 ± 0.02	38.4%	3.39 ± 0.07	23.5%

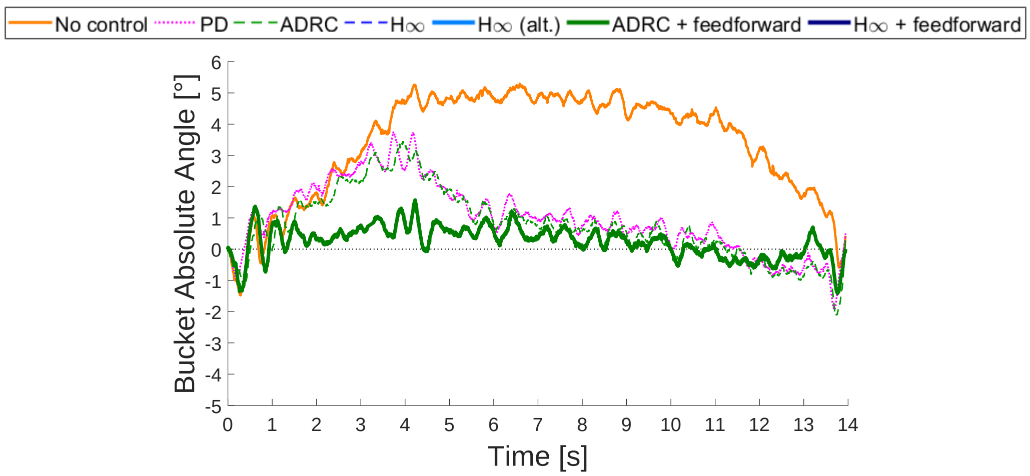

(A) Low speed (ADRC).

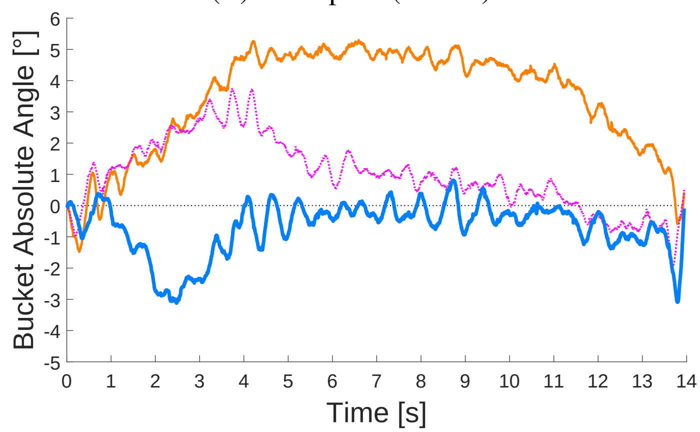

(B) Low speed (alternative $\mathcal{H}_\infty$).

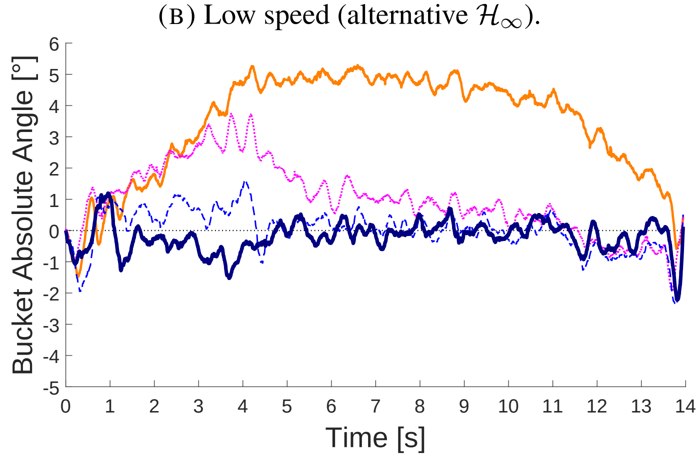

(C) Low speed ($\mathcal{H}_\infty$).

FIGURE 5.7. Experimental results driving the robotic loader over a ramp at low speed.

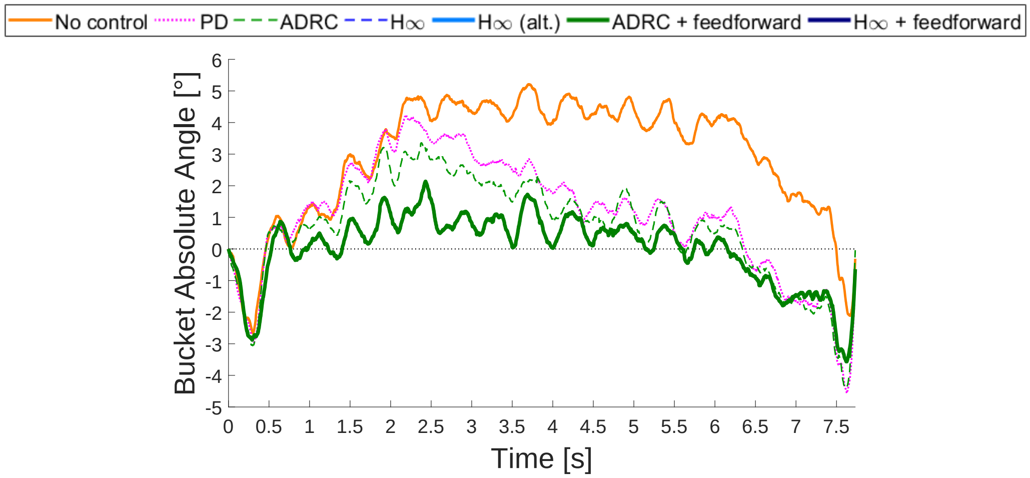

(A) Low speed (ADRC).

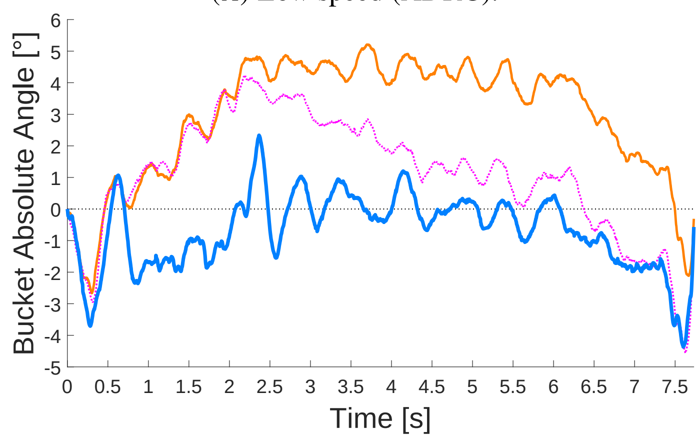

(B) Low speed (alternative $\mathcal{H}_\infty$).

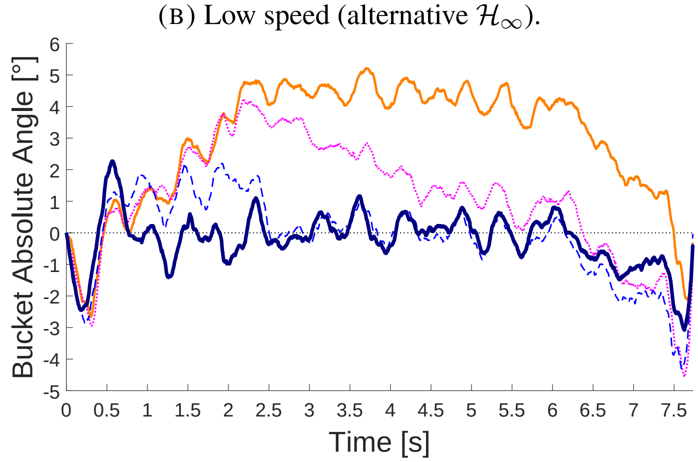

(C) Low speed ($\mathcal{H}_\infty$).

FIGURE 5.8. Experimental results driving the robotic loader over a ramp at high speed.

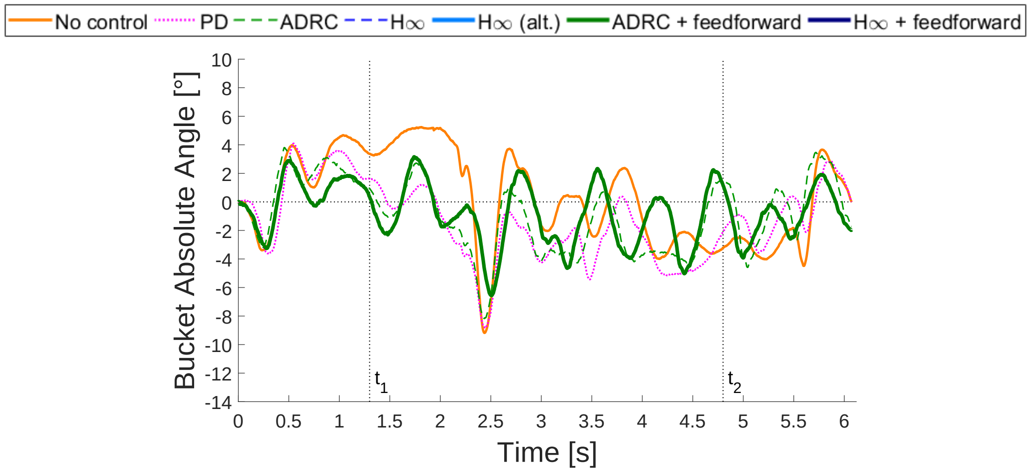

(A) Low speed (ADRC).

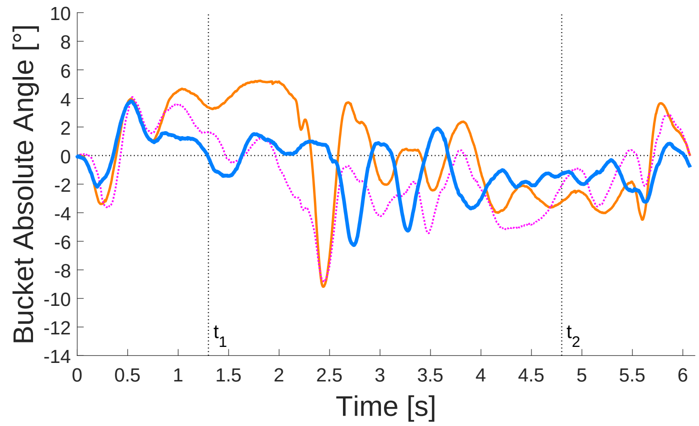

(B) Low speed (alternative $\mathcal{H}_\infty$).

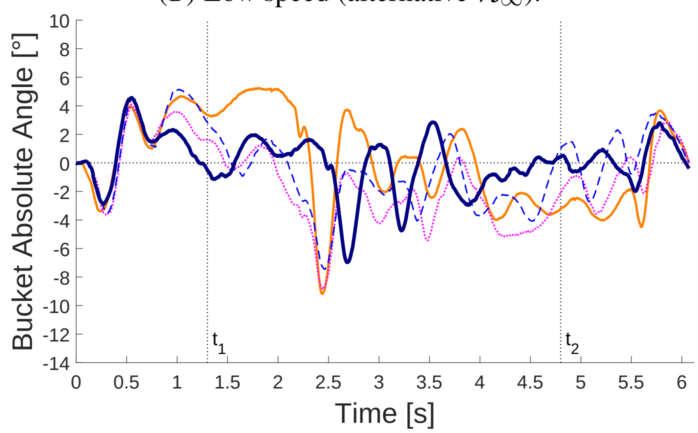

(C) Low speed ($\mathcal{H}_\infty$).

FIGURE 5.9. Experimental results driving the robotic loader over a road bump at low speed.

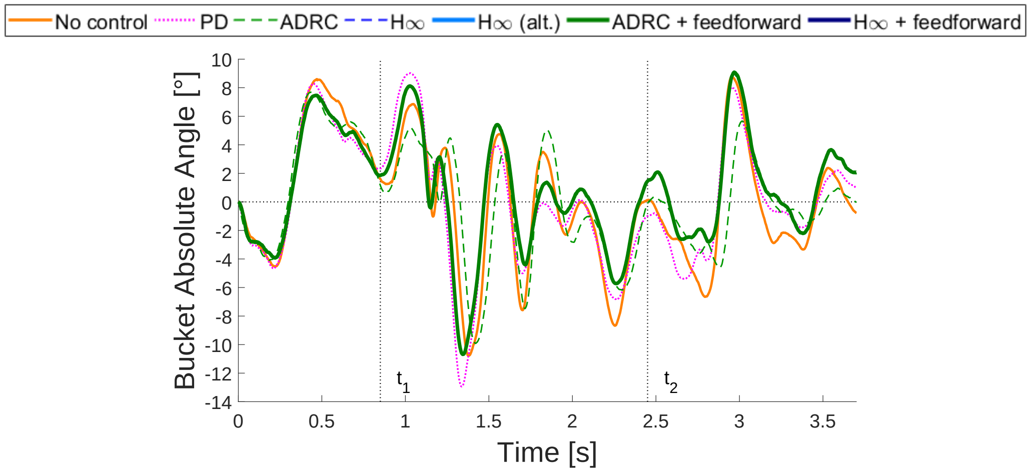

(A) High speed (ADRC).

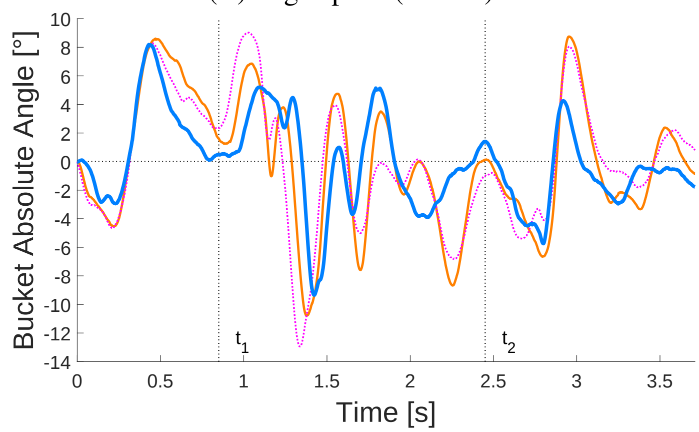

(B) High speed (alternative $\mathcal{H}_\infty$).

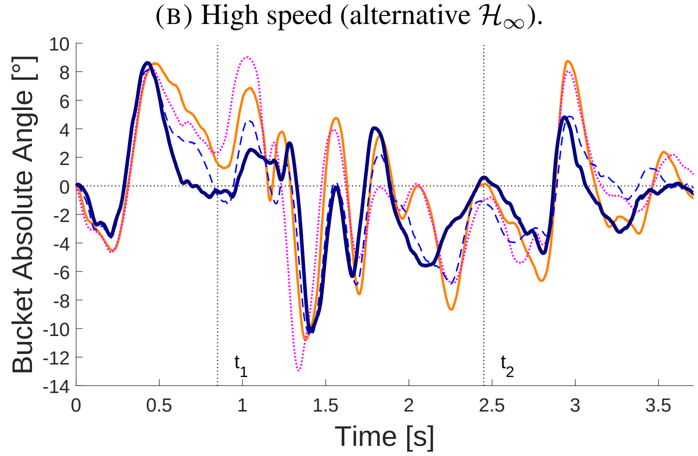

(C) High speed ($\mathcal{H}_\infty$).

FIGURE 5.10. Experimental results driving the robotic loader over a road bump at high speed.

5.3. Discussion

It is noted that in spite of the model's complexity and its parameter uncertainty, the simulation results are reasonably consistent with those obtained during experiments with the industrial skid-steer loader. The trajectories followed by the bucket tilt during the ramp experiments are consistent between simulations and tests on the real equipment for the different control schemes. Discrepancies become significant for the road bump experiments, especially at higher speeds, due to the factors discussed in Chapter 4. For this reason, the experiment results on the real machine tend to be worse than those obtained from simulations. But to some extent, the discussed dynamic model for a hydraulically actuated mobile manipulator is able to accurately represent the effect of terrain disturbances and control input on the position of the end-effector, and when this does not hold the sources of error have been identified.

In general terms, all implemented control schemes are able to reduce the effect of terrain disturbances on the position of the end-effector bucket tilt, with the proposed control scheme combining $\mathcal{H}_\infty$ control with feedforward performing best. The $\mathcal{H}_\infty$ control on its own is already effective in reducing the effect of disturbances, but the introduction of feedforward action greatly improves results, particularly in eliminating the low frequency component of the end-effector position error.

Regarding the ADRC method, it at least improves upon the PD controller used for reference, with a noticeable increase in disturbance reduction at higher speed. Results for the ADRC are very similar to those obtained by the $\mathcal{H}_\infty$ control on simulations, particularly for the road bump experiments at high speed, though performance becomes noticeably worse than the $\mathcal{H}_\infty$ control on the real equipment, possibly due to the system's non-minimum phase characteristics. Performance could improve if a greater order model were used to build the extended state observer, as a better estimate should be obtained for the disturbance term fed to the controller. This would also require estimating more parameters, which goes somewhat against the core concept of ADRC of representing the system with a simple model and estimating the unmodeled higher order dynamics through the extended state observer. This concept is what motivated its use in this work, and despite having worse performance than the $\mathcal{H}_\infty$ control in this evaluation, with the exception of the simulations with a loaded bucket, the mentioned trade-off between performance and design simplicity may be acceptable in some applications.

Concerning the alternative $\mathcal{H}_\infty$ controller which considers measurements from both sensors instead of using the base pitch rate to compute the feedforward action, performance effectively increases for higher frequency disturbances compared to the proposed method, as observed during the high speed road bump experiments. Nonetheless, as it heavily weighs the measured vehicle base pitch rate compared to the measured bucket tilt when computing the control input, and the model it is based on presents discrepancies with the real equipment, it tends to perform poorly at low frequencies and presents steady-state error near the reference.

Lastly, due to construction aspects of the studied equipment and the dynamic characteristics of the actuators used for control, any attempt to significantly reduce the effect of higher frequency disturbances will be limited. As discussed in Chapter 4, the non-rigidity of the studied manipulator's arm links, among other factors, results in high amplitude oscillations of the end-effector when the vehicle base experiences high frequency accelerations. In order to successfully counter these high amplitude oscillations, aggressive control action would be required, but as it was also discussed in Chapter 4, this introduces even more oscillatory behavior on the end-effector position.

6. CONCLUSION AND FUTURE RESEARCH

6.1. Review of the Results and General Remarks

A control approach relying on $\mathcal{H}_\infty$ control together with a feedforward law to reduce the propagation of terrain disturbances to the end-effectors of mobile robotic manipulators was presented. The disturbance rejection approach is compared to a standard PD controller and an Active Disturbance Rejection Control (ADRC), as well as to an alternative $\mathcal{H}_\infty$ control structure which considers multiple sensor measurements for output feedback instead of using a feedforward law. The approach was evaluated on simulations and validated experimentally using a semi-autonomous Cat®262C compact skid-steer loader equipped with inclination and inertial sensors.

The results showed consistency between the simulated and experimental data. In general, the best results were obtained using the proposed approach. The proposed control scheme reduces terrain disturbances RMSE metrics around 86% and 74% when traversing a 4 m long ramp at 12.5% and 25% of maximum vehicle speed, respectively. Similarly, reductions of 38% and 24% are obtained when traversing typical mound or rock sizes at the same speeds. The performance of the proposed scheme for the mound experiments at high speed was slightly worse than that of the alternative $\mathcal{H}_\infty$ control scheme which integrated measurements from bucket tilt and base pitch rate. Nonetheless, this alternative scheme performed worse at low speeds and presented steady-state errors, thus rendering it as an inferior solution in general terms. Other tested schemes, such as the manually tuned standard PD controller and ADRC performed worse. The omission of feedforward action was also tested experimentally, and was proven to worsen the performance of the proposed scheme.

The ability of the proposed strategy to reduce the terrain induced disturbances is limited by the reaction time and response characteristics of the actuators. Control performance is also limited by cantilever oscillations of the manipulator arm, which are intrinsic of the machine used for experiments. Despite this limitations, the approach can be useful to minimize the loss of material during haul in mining operations by mobile robotic manipulators. This is currently a problem even in remotely operated sites, in which the material that falls from the bucket of one of the load-haul and dump vehicles causes the following vehicles in the convoy to lose part of their load when the machine drives over the fallen rocks that the teleoperator is not able to clearly see on the control interface and avoid. Even though this approach has been validated for a specific machine, it should be easily adaptable to other mobile robotic manipulators used in this context due to the state-space representation defined in this work, and provided that the model parameters used for control design are adequately adjusted.

6.2. Future Research Topics

Future research topics include the evaluation of the proposed control scheme on different equipment, refinement of the proposed disturbance compensation strategy to minimize energy consumption, motion optimization using multiple joints simultaneously for reference tracking on more dimensions, as well as the exploration of long range scanning of the road surface using lidar sensors to improve the controller response at higher driving speeds.

It is also of interest to compare the performance of the proposed approach with existing passive terrain disturbance rejection solutions. It is not clear whether combining a passive solution with an active approach could yield better disturbance rejection results by exploiting the good performance of the passive solution at high frequencies, complemented by the good response of the actuators at lower frequencies.

References

Aguilera-Marinovic, S., & Torres-Torriti, M. (2014, February). *Caterpillar 262C skid-steer loader model and simulation files for the Spatial Vector Algebra toolbox by Roy Featherstone.* http://ral.ing.puc.cl/ssmm.htm.

Aguilera-Marinovic, S., Torres-Torriti, M., & Auat-Cheein, F. (2017, Feb). General dynamic model for skid-steer mobile manipulators with wheel-ground interactions. *IEEE/ASME Trans. Mechatronics*, *22*(1), 433-444. doi: 10.1109/TMECH.2016.2601308

A'Hearn, M. A., Carlson, D. J., Hajek, T. J., Hatcher, A., Hudson, M. D., Quinn, P., & Tolappa, S. T. (2002, Mar). *Hydraulic ride control system.*

Azad, M., & Featherstone, R. (2014, June). A new nonlinear model of contact normal force. *IEEE Trans. Robot.*, *30*(3), 736-739. doi: 10.1109/TRO.2013.2293833

Balas, G., Chiang, R., Packard, A., & Safonov, M. (2015). Robust control toolbox users guide [Computer software manual]. Natick, MA, USA.

Caterpillar. (n.d.). *How haul road maintenance can extend tire life.* https://www.cat.com/en_US/by-industry/mining/articles/haul-road-maintenance.html.

Caterpillar. (2013, October). *New CAT® D series skid steer loaders feature new cab, operator environment and control and increased engine performance.* https://www.cat.com/en_IN/news/machine-press-releases/new-cat-d-seriesskidsteerloadersfeaturenewcaboperatorenvironment.html.

Caterpillar. (2016, July). *Speed sensitive ride control for Cat® D/D2 series skid steer, multi terrain, compact track loaders.* `https://www.youtube.com/watch?v=-KQNAsrgDM0`.

Caterpillar. (2017, January). *New D series AG handlers feature power choices, load-sensing hydraulics, operator comfort, and exceptional versatility.* `https://www.cat.com/en_IN/news/machine-press-releases/new-d-series-ag-handlers-feature-power-choices-load-sensing-hydraulics-operator-comfort-and-exceptional-versatility.html`.

Chi-Wu, B., & Ke-Fei, X. (2009, July). Robust control of mobile manipulator service robot using torque compensation. In *2009 international conference on information technology and computer science* (Vol. 2, p. 69-72). doi: 10.1109/ITCS.2009.152

Doyle, J., Glover, K., Khargonekar, P., & Francis, B. (1989). State-space solutions to standard $\mathcal{H}_2$ and $\mathcal{H}_\infty$ control problems. *IEEE Transactions on Automatic Control*, *34*(8), 831–847. doi: 10.1109/9.29425

Dubowsky, S., & Tanner, A. B. (1987). A study of the dynamics and control of mobile manipulators subjected to vehicle disturbances. In *Proc. of 4th int. symp. of robotics research* (p. 111-117).

Efe, Y. (2014). *Dynamic model of a hydraulic servo system for a manipulator robot* (Unpublished master's thesis). KTH, Electrical Energy Conversion.

Fales, R., & Kelkar, A. (2005, June). Robust control design for a wheel loader using mixed sensitivity H-infinity and feedback linearization based methods. In *Proceedings of the 2005, american control conference, 2005.* (p. 4381-4386 vol. 6). doi: 10.1109/ACC.2005.1470669

Featherstone, R. (2008). Spatial vector algebra. In *Rigid body dynamics algorithms* (pp. 7–38). Springer US. Retrieved from https://doi.org/10.1007/978-1-4899-7560-7_2 doi: 10.1007/978-1-4899-7560-7_2

Featherstone, R. (2012, June). Spatial vector and rigid-body dynamics software. version 2.0 [Computer software manual]. (URL: http://royfeatherstone.org/spatial/v2/)

Gao, Z. (2003, June). Scaling and bandwidth-parameterization based controller tuning. In *Proceedings of the 2003 american control conference, 2003.* (Vol. 6, p. 4989-4996). doi: 10.1109/ACC.2003.1242516

Gao, Z. (2006, June). Active disturbance rejection control: A paradigm shift in feedback control system design. In *2006 american control conference.* doi: 10.1109/ACC.2006.1656579

Gilardi, G., & Sharf, I. (2002). Literature survey of contact dynamics modelling. *Mechanism and Machine Theory*, *37*(10), 1213 - 1239. Retrieved from http://www.sciencedirect.com/science/article/pii/S0094114X02000459 doi: http://dx.doi.org/10.1016/S0094-114X(02)00045-9

Glover, K., & Doyle, J. C. (1988, September). State-space formulae for all stabilizing controllers that satisfy an $\mathcal{H}_\infty$-norm bound and relations to relations to risk sensitivity. *Systems & Control Letters*, *11*(3), 167–172. doi: 10.1016/0167-6911(88)90055-2

Gustafson, A. (2011). *Automation of load haul dump machines* (Tech. Rep.). Lulea University of Technology.

Han, J. (2009, March). From PID to active disturbance rejection control. *IEEE Trans. Ind. Electron.*, *56*(3), 900-906. doi: 10.1109/TIE.2008.2011621

Hatano, M., Ohsumi, T., Minami, M., & Asakura, T. (2000). Motion control of mobile manipulators traveling on irregular terrain dentification of shape of terrain using GA and inverse dynamics compensation. In *2000 TENCON proceedings. intelligent systems and technologies for the new millennium.* IEEE. doi: 10.1109/tencon.2000.888396

Holman, P. (2006). *Caterpillar® haul road design and management.* Big Iron University, St. Charles, IL.

Hootsmans, N. A. M., & Dubowsky, S. (1991, Apr). Large motion control of mobile manipulators including vehicle suspension characteristics. In *Proceedings. 1991 ieee int. conf. robot. and automation* (p. 2336-2341 vol.3). doi: 10.1109/ROBOT.1991.131751

Jimenez-Lozano, J., & Goodwine, B. (2011). Nonlinear disturbance decoupling for a mobile robotic manipulator over uneven terrain. In *IFAC proceedings* (Vol. 44, p. 6930 - 6936). Retrieved from `http://www.sciencedirect.com/science/article/pii/S147466701644718X` doi: https://doi.org/10.3182/20110828-6-IT-1002.00566

Larsson, J., Appelgren, J., & Marshall, J. (2010). Next generation system for unmanned LHD operation in underground mines. In *Proc. of the annual meeting and exhibition of the society for mining, metallurgy & exploration.*

Mattila, J., Koivumki, J., Caldwell, D. G., & Semini, C. (2017, April). A survey on control of hydraulic robotic manipulators with projection to future trends. *IEEE/ASME Transactions on Mechatronics*, *22*(2), 669-680. doi: 10.1109/TMECH.2017.2668604

Ningyue, Liyan, & Liukeping. (2015, Nov). The research of mobile manipulator trajectory tracking cooperative control based on the ADRC. In *2015 chinese automation congress* (p. 385-389). doi: 10.1109/CAC.2015.7382530

Paraszczak, J., Gustafson, A., & Schunnesson, H. (2015). Technical and operational aspects of autonomous LHD application in metal mines. *Int. Journal of Mining, Reclamation and Environment*, *29*(5), 391-403. Retrieved from `http://www.tandfonline.com/doi/abs/10.1080/17480930.2015.1086553` doi: 10.1080/17480930.2015.1086553

Perrier, C., Cellier, L., & Dauchez, P. (1997). Experimental comparison of hybrid and external control structures for a mobile manipulator. In *Proceedings of international conference on robotics and automation.* IEEE. doi: 10.1109/robot.1997.606889

Senyard, M. (2010, September). *Haul road maitenance: A vital factor in the value chain.* `https://www.agg-net.com/files/aggnet/attachments/articles/haul_road_maintenance_0.pdf`.

Toivonen, H. T. (1998). *Robust control methods.* Äbo Akademi University, Turku, Finland.

Yang, X., Zheng, X., & Chen, Y. (2018, Feb). Position tracking control law for an electro-hydraulic servo system based on backstepping and extended differentiator. *IEEE/ASME Transactions on Mechatronics*, *23*(1), 132-140. doi: 10.1109/TMECH.2017.2746142

Yung, I., Vázquez, C., & Freidovich, L. (2015). Automation of front end loaders: Self leveling task. In *Ieee 20th conf. on emerging technologies factory automation* (p. 1-7). doi: 10.1109/ETFA.2015.7301451

Zames, G. (1981, April). Feedback and optimal sensitivity: Model reference transformations, multiplicative seminorms, and approximate inverses. *IEEE Transactions on Automatic Control*, *26*(2), 301-320. doi: 10.1109/TAC.1981.1102603

Zhou, K., Doyle, J., & Glover, K. (1996). *Robust and optimal control*. Upper Saddle River, NJ, USA: Prentice-Hall, Inc.

APPENDICES

APPENDIX A. CONTROL ROBUSTNESS EVALUATION

In practice, accurately estimating all model parameters is a very difficult task and thus the system's dynamics are better represented by a set of models. The computed controller may not be optimal for all models belonging to this uncertainty set, but system stability should at least be guaranteed. It is also of interest to study the closed loop system's performance for different model parameters, and thus quantify its robustness to model uncertainty. The following sections will briefly present the theory behind the μ-analysis method for evaluation of robust stability and performance (Zhou, Doyle, & Glover, 1996) of a closed loop system, along with an evaluation of the designed controller's robustness to model uncertainties, using the mentioned method.

A.1. Structured Singular Value and System Robustness Evaluation

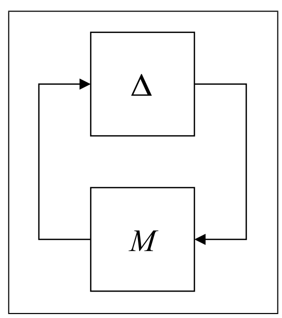

FIGURE A.1. Standard feedback system $\boldsymbol{M}\Delta$.

Given the standard feedback system shown in Fig. A.1, with stable blocks $\boldsymbol{M}$ and Δ, by small-gain theorem, the system is stable if:

$$\|\boldsymbol{M}\|_\infty \cdot \|\Delta\|_\infty < 1 \tag{A.1}$$

Now, let Δ correspond to a structured uncertainty matrix, with $\boldsymbol{\Delta}$ all admitted uncertainty matrices which follow a normalized uncertainty sctructure such that $\|\Delta\|_\infty = 1$ represents an upper bound for admitted uncertainties. The structured singular value is thus defined as:

$$\mu_{\boldsymbol{\Delta}}(\boldsymbol{M}) = \frac{1}{\min\{\bar{\sigma}(\Delta) : \Delta \in \boldsymbol{\Delta}, \det(\boldsymbol{I} - \boldsymbol{M}\Delta) = 0\}} \tag{A.2}$$

that is, the reciprocal of the smallest structured uncertainty Δ for which the system becomes unstable. Following the above logic, the uncertain system is stable for all uncertainties $\Delta \in \boldsymbol{\Delta}$ if for all frequencies:

$$\mu_{\boldsymbol{\Delta}}(\boldsymbol{M}) < 1 \tag{A.3}$$

From condition (A.3), and the shaping of respective matrix $\boldsymbol{M}$, the robust stability and performance of an uncertain system may be analized. For the case of robust stability, consider the closed-loop system with multiplicative uncertainty Δ presented in Fig. A.2a. This system can be represented in the $\boldsymbol{M}\Delta$ form, as shown in Fig. A.2b. Thus from the structured singular value condition, system robust stability is guaranteed if for all frequencies:

$$\mu_{\boldsymbol{\Delta}}(\boldsymbol{GK}\,(\boldsymbol{I}+\boldsymbol{GK})^{-1}) < 1 \tag{A.4}$$

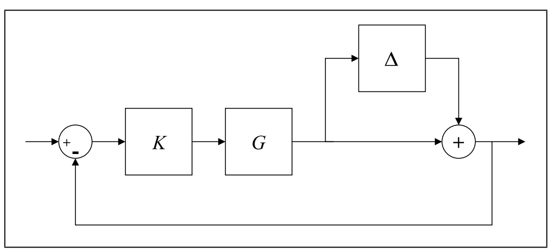

(A) Closed-loop system with multiplicative uncertainty.

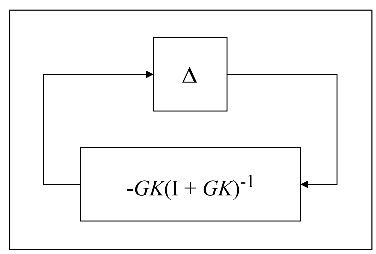

(B) $\boldsymbol{M}\Delta$ representation for robust stability analysis.

FIGURE A.2. Uncertain closed loop representation for robust stability analysis.

For the case of robust performance, consider the closed-loop system with an additive output uncertainty presented in Fig. A.3a. Notice that the system connected to the left hand of the uncertainty block $\Delta_{\boldsymbol{S}}$ corresponds to the output sensitivity function $\boldsymbol{S}$, which may be used to measure the performance of the closed-loop system. A measure for robust performance is such that if for all frequencies, the uncertain system satisfies:

$$\|\boldsymbol{S}\|_{\infty} < 1 \tag{A.5}$$

That is, if output disturbances have less than unitary gain. This is analogous to the small-gain theorem for robust stability but applied as a measure for robust performance. In a similar fashion, this system may be represented in the $M\Delta$ form, as shown in Fig. A.3b. Thus from the structured singular value condition, system robust performance is guaranteed if the structured singular value of the bottom block from Fig. A.3b related to system sensitivity is less than 1 for all frequencies.

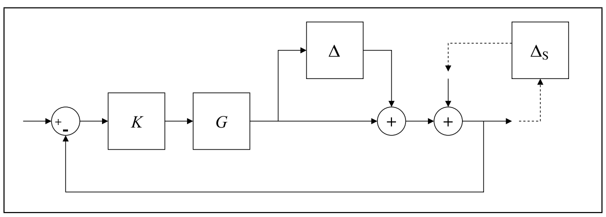

(A) Closed-loop system with additive output uncertainty.

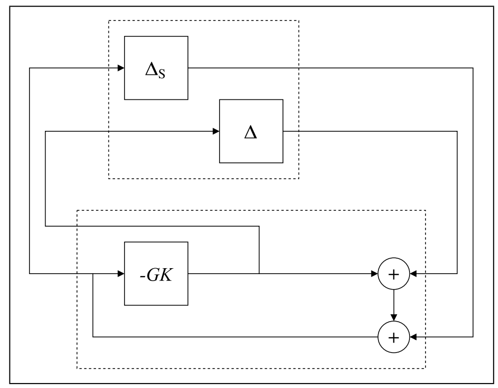

(B) $M\Delta$ representation for robust performance analysis.

FIGURE A.3. Uncertain closed loop representation for robust performance analysis.

A.2. Proposed Controller Robustness Evaluation

The servovalve response time T_v and the dampened spring-like force coefficients K_C, D_C for the manipulator's first link are the main uncertain parameters of the model which may have an influence on the resulting closed-loop system dynamics. Thus, the closed-loop robustness is evaluated for variations of T_v from 0.1s to 0.2s and variations of the pair K_C, D_C such that the natural oscillation frequency of the manipulator arm is within 1.2 Hz and 2.0 Hz. The resulting open and closed-loop responses of the first component of $\boldsymbol{z}_\infty$ to an input disturbance $a_{1,\theta}$, with nominal and uncertain system parameters, are presented in Fig. A.4.

The structured singular values for both robust stability and performance are computed for the mentioned uncertainties and presented in Fig. A.5. The $\mu < 1$ criteria for robust stability, as detailed in (Zhou et al., 1996), is satisfied. The robust performance analysis shows that for most frequencies the controller's disturbance rejection is robust to model

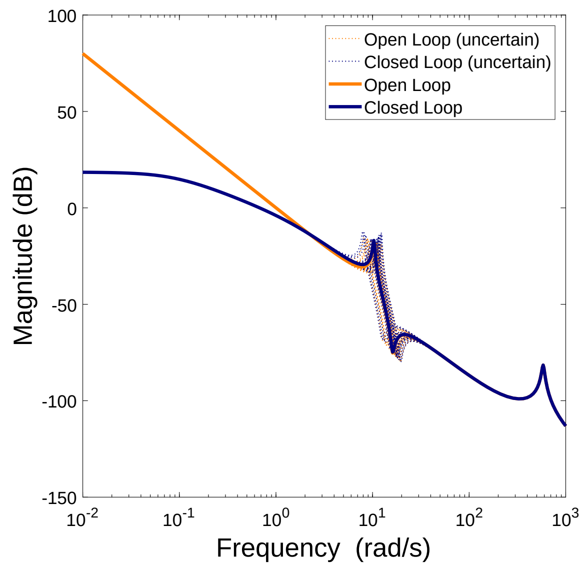

FIGURE A.4. Open and closed-loop response of the first component of $\boldsymbol{z}_{\infty}$ for input disturbance $a_{1,\theta}$ (with uncertain parameters).

uncertainty, except within a limited range of frequencies between 5.5 and 13 rad/s where the upper bound of the structured singular value is $1 < \mu < 1.62$. Thus, for the mentioned uncertain parameters, system stability is ensured and the system worst case gain is guaranteed less than 1.62 over a limited frequency range, and less than 1 over all remaining frequencies.

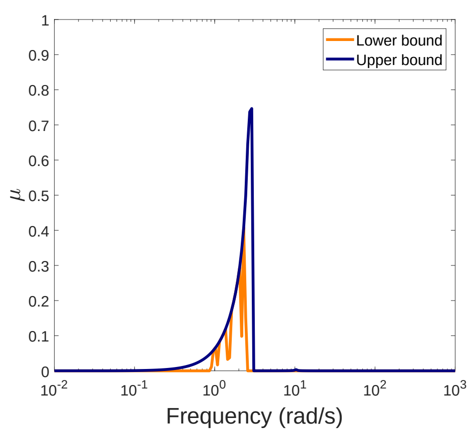

(A) Robust stability.

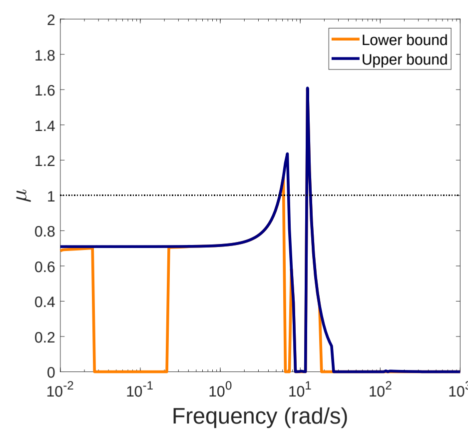

(B) Robust performance.

FIGURE A.5. Closed-loop structured singular values.

APPENDIX B. COMPLETE EXPERIMENTAL RESULTS

The complete set of test experiments carried out on the industrial compact skid-steer loader Cat®262C for each control scheme, which were used to compute the mean performance metrics, are presented. Each curve represents one of the three experimental tests for each control scheme.

B.1. Ramp Experiments

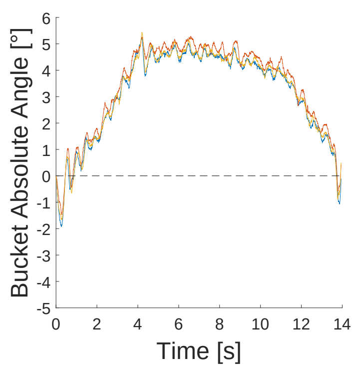

(A) 12.5% max. vehicle speed.

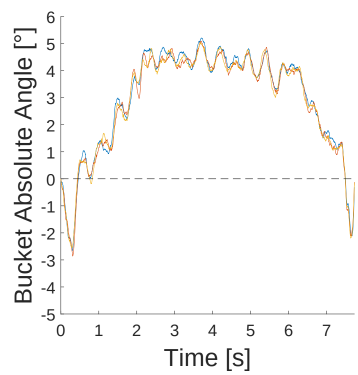

(B) 25% max. vehicle speed.

FIGURE B.1. No control results over ramp.

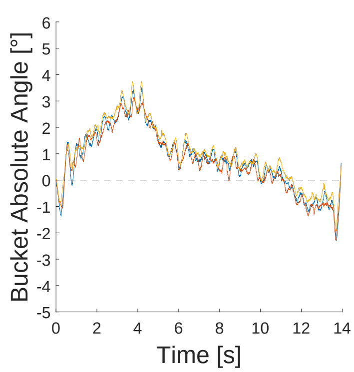

(A) 12.5% max. vehicle speed.

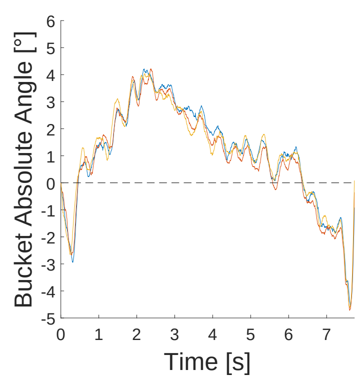

(B) 25% max. vehicle speed.

FIGURE B.2. PD results over ramp.

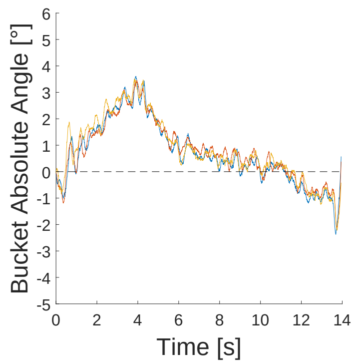

(A) 12.5% max. vehicle speed.

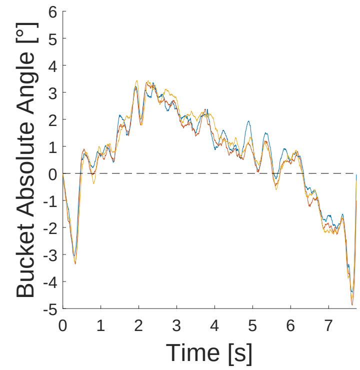

(B) 25% max. vehicle speed.

FIGURE B.3. ADRC results over ramp.

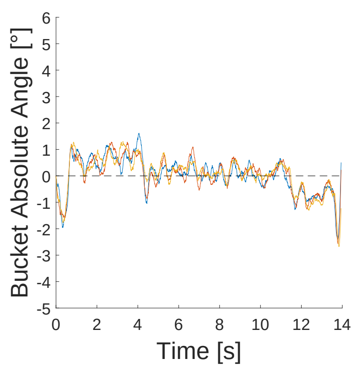

(A) 12.5% max. vehicle speed.

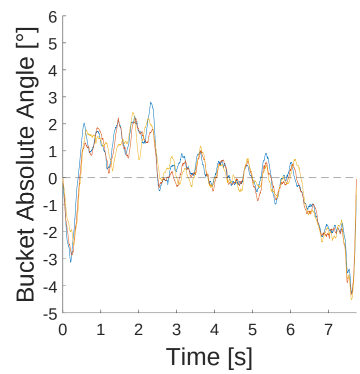

(B) 25% max. vehicle speed.

FIGURE B.4. $\mathcal{H}_\infty$ results over ramp.

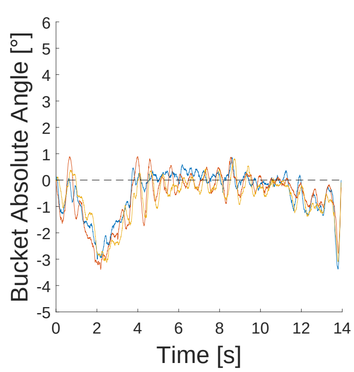

(A) 12.5% max. vehicle speed.

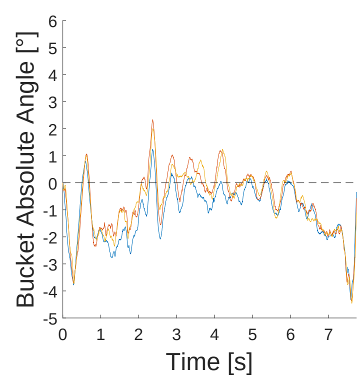

(B) 25% max. vehicle speed.

FIGURE B.5. Alternate $\mathcal{H}_\infty$ results over ramp.

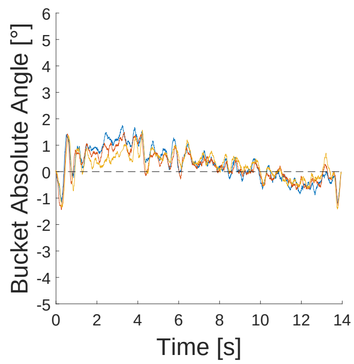

(A) 12.5% max. vehicle speed.

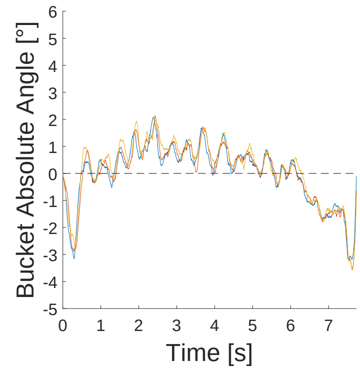

(B) 25% max. vehicle speed.

FIGURE B.6. ADRC + feedforward results over ramp.

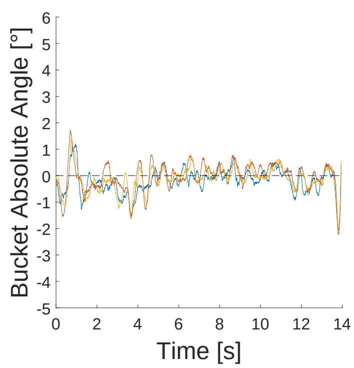

(A) 12.5% max. vehicle speed.

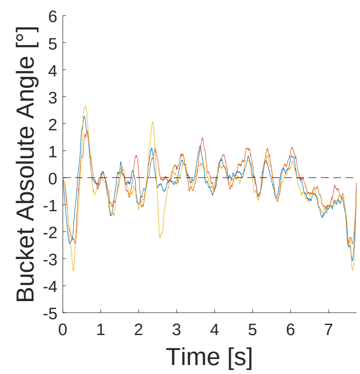

(B) 25% max. vehicle speed.

FIGURE B.7. $\mathcal{H}_\infty$ + feedforward results over ramp.

B.2. Road Bump Experiments

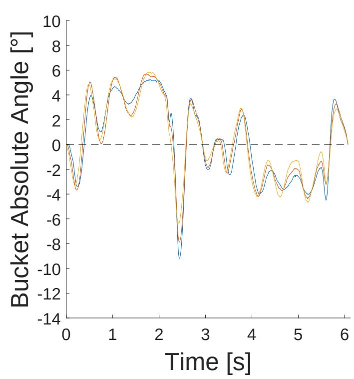

(A) 12.5% max. vehicle speed.

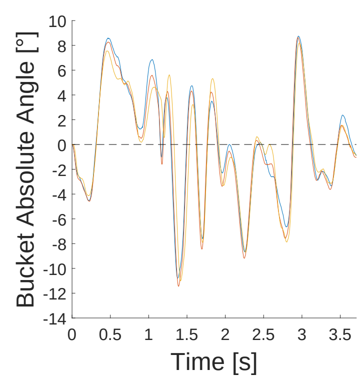

(B) 25% max. vehicle speed.

FIGURE B.8. No control results over bump.

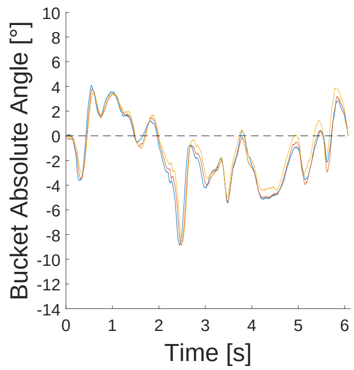

(A) 12.5% max. vehicle speed.

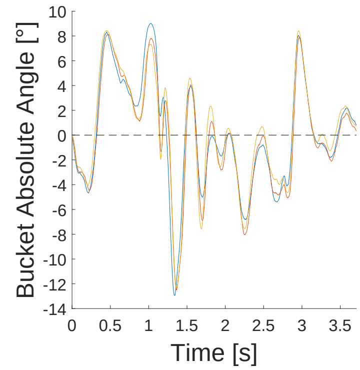

(B) 25% max. vehicle speed.

FIGURE B.9. PD results over bump.

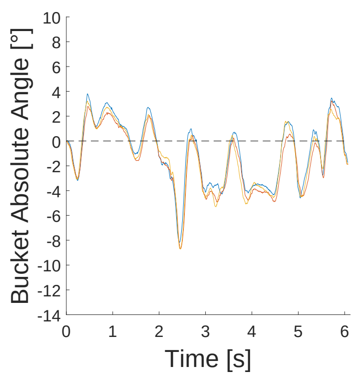

(A) 12.5% max. vehicle speed.

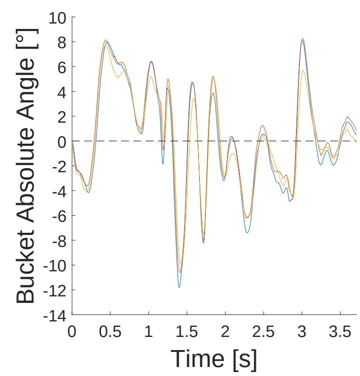

(B) 25% max. vehicle speed.

FIGURE B.10. ADRC results over bump.

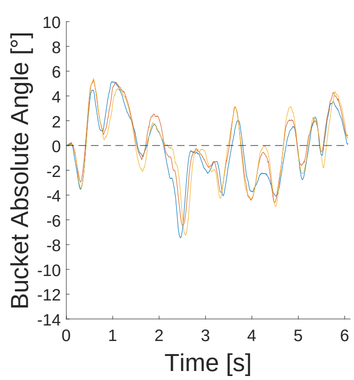

(A) 12.5% max. vehicle speed.

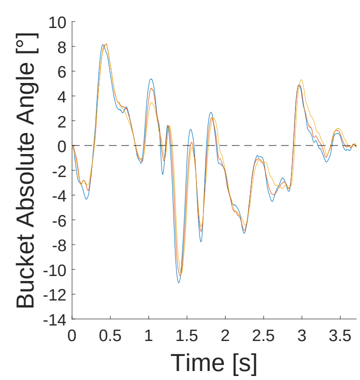

(B) 25% max. vehicle speed.

FIGURE B.11. $\mathcal{H}_\infty$ results over bump.

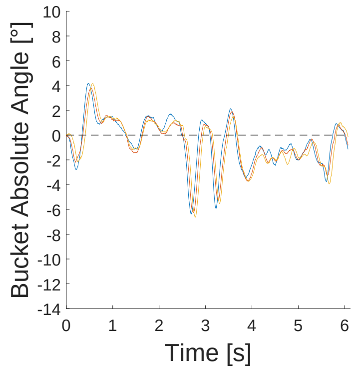

(A) 12.5% max. vehicle speed.

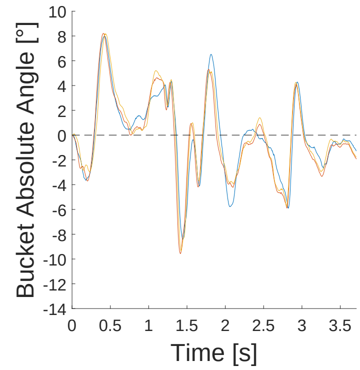

(B) 25% max. vehicle speed.

FIGURE B.12. Alternate $\mathcal{H}_\infty$ results over bump.

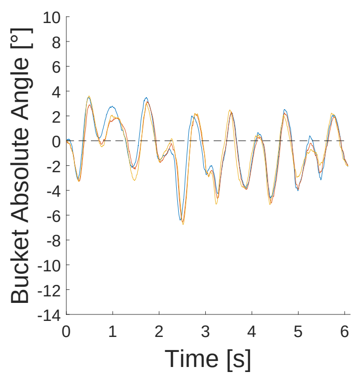

(A) 12.5% max. vehicle speed.

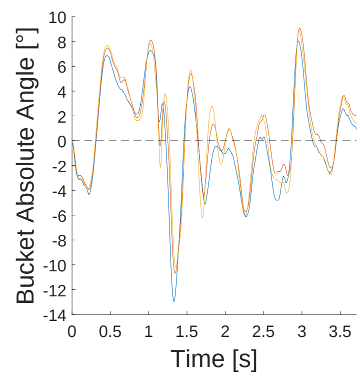

(B) 25% max. vehicle speed.

FIGURE B.13. ADRC + feedforward results over bump.

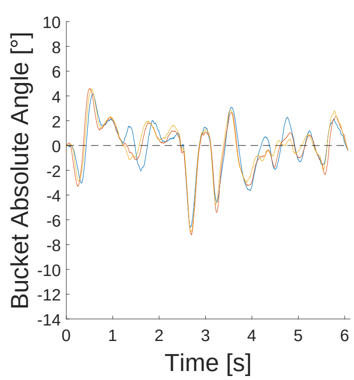

(A) 12.5% max. vehicle speed.

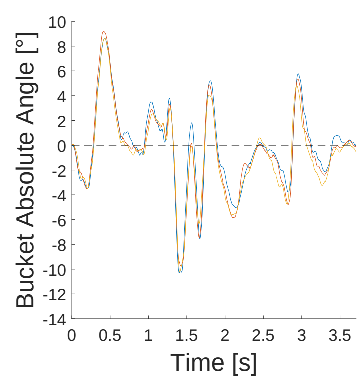

(B) 25% max. vehicle speed.

FIGURE B.14. $\mathcal{H}_\infty$ + feedforward results over bump.